



**HAL**  
open science

## Host-Guest Silicalite-1 Zeolites: Correlated Disorder and Phase Transition Inhibition by a Small Guest Modification

Marco Fabbiani, Shadi Al-Nahari, Laura Piveteau, Eddy Dib, Vasyl Veremeienko, Arnold Gaje, Dan G Dumitrescu, Philippe Gaveau, Tzonka Mineva, Dominique Massiot, et al.

► **To cite this version:**

Marco Fabbiani, Shadi Al-Nahari, Laura Piveteau, Eddy Dib, Vasyl Veremeienko, et al.. Host-Guest Silicalite-1 Zeolites: Correlated Disorder and Phase Transition Inhibition by a Small Guest Modification. *Chemistry of Materials*, 2022, 34 (1), pp.366-387. 10.1021/acs.chemmater.1c03721 . hal-03507387

**HAL Id: hal-03507387**

**<https://hal.science/hal-03507387>**

Submitted on 3 Jan 2022

**HAL** is a multi-disciplinary open access archive for the deposit and dissemination of scientific research documents, whether they are published or not. The documents may come from teaching and research institutions in France or abroad, or from public or private research centers.

L'archive ouverte pluridisciplinaire **HAL**, est destinée au dépôt et à la diffusion de documents scientifiques de niveau recherche, publiés ou non, émanant des établissements d'enseignement et de recherche français ou étrangers, des laboratoires publics ou privés.

# Host-Guest MFI Zeolites: Correlated Disorder and Phase Transition Inhibition by a Small Guest Modification

Marco Fabbiani,<sup>a</sup> Shadi Al-Nahari,<sup>a</sup> Laura Piveteau,<sup>b</sup> Eddy Dib,<sup>a,#</sup> Vasyl Veremeienko,<sup>a</sup> Arnold Gaje,<sup>a,§</sup> Dan G. Dumitrescu,<sup>c</sup> Philippe Gaveau,<sup>a</sup> Tzonka Mineva,<sup>a</sup> Dominique Massiot,<sup>b</sup> Arie van der Lee,<sup>d</sup> Julien Haines<sup>a</sup> and Bruno Alonso<sup>a,\*</sup>

<sup>a</sup> ICGM, Université de Montpellier, CNRS, ENSCM, Montpellier, France

<sup>b</sup> CNRS, CEMHTI UPR3079, Univ. Orléans, Orléans, France

<sup>c</sup> Elettra, Sincrotrone Trieste S.C.p.A., Basovizza, Trieste, 34149, Italy

<sup>d</sup> IEM, Université de Montpellier, CNRS, ENSCM, Montpellier, France

\* E-mail: bruno.alonso@enscm.fr

Present Addresses:

#E.D.: Laboratoire Catalyse & Spectrochimie, Normandie Univ, ENSICAEN, UNICAEN, CNRS, 14000 Caen, France

§A.G.: Department of Chemistry, College of Arts and Sciences, University of the Philippines Visayas, 5023 Miag-ao, Iloilo, Philippines

## ABSTRACT

We have investigated the nature and extent of nanoscale disorder in prototypical host-guest zeolites, made of silicalite-1 (host) and organic structure directing agent (OSDA, guest). The four different selected OSDA-silicalite-1 differ in: the mineralizing agent used ( $F^-$  vs.  $OH^-$ ), the synthesis' method (hydrothermal vs. solvent-free) and the OSDA (tetrapropylammonium TPA vs. tripropylethylammonium TPEA). The comparison between TPA and TPEA, chemically similar but differing in their symmetry, is examined in great detail owing to the novel relationship found between the geometrical disorder and the monoclinic-orthorhombic (m-o) phase transition occurring at low temperature. Long- and short-range organization and ordering are characterized by complementary XRD, Raman and multinuclear NMR ( $^{13}C$ ,  $^{14}N$ ,  $^{29}Si$ ). The possibility of the m-o transition is studied by all these techniques at variable low  $T$ . An in-depth study of the disorder is carried out by x-ray structure determination and 2D NMR  $^{29}Si$ - $^{29}Si$  INADEQUATE correlations, including an up-to-date analysis of anisotropic atomic displacement parameters and a new fitting approach to estimate correlated disorder from 2D NMR datasets. The collected results allow to demonstrate how the disorder created by the positioning of the less symmetric TPEA guest leads to a correlated geometrical disorder for half of the atom sites in the host framework that completely inhibits the m-o phase transition.

## INTRODUCTION

Microporous crystalline zeolite materials are currently used for multiple applications owing to the possible combinations of their specific properties like molecular shape selectivity, adsorption and reactivity.<sup>1-7</sup> Interestingly, zeolites might exhibit internal disorder, of different nature and extent, that will affect their final properties. Disorder can arise from crystal defects coming typically from a non-ordered stacking of layers, structure intergrowth, twinning, or a reduced dimensionality. For instance, the crystal disorder of zeolite SSZ-57 – a structure presenting a MEL topology interrupted by disordered regions containing 12 membered rings (MR) –<sup>8</sup> leads to pore filling properties that can be further exploited for heterogeneous catalysis (cracking, isomerization) by selective positioning of Al<sup>3+</sup> and B<sup>3+</sup> cations in the large (12 MR) and intermediate (10 MR) pores respectively.<sup>9</sup> More recently, the new zeolite PST-24, possessing randomly dispersed open and closed valves, presents local variations in channel dimensionality and high yields for the production of butadiene from 1,3-butanediol.<sup>10</sup> Further, interesting and improved catalytic performances have been demonstrated for several 2D zeolites possessing a faster molecular diffusion to active sites, but the high impact of the presence of these sites at the more disordered external crystal surface has also been recognized.<sup>11</sup> Using an assembly–disassembly–organization–reassembly (ADOR) route, it has also been shown that the internal surface area, and the related adsorptive properties, can be continuously tuned by varying the stacking of layered intermediates in a statistical, and thus non-ordered, fashion.<sup>12</sup>

Disorder arises also from defects of chemical nature like the non-ordered distribution in M<sup>3+</sup> cations or the presence of broken bonds and connectivity defects. The degree of ordering in the distributions of Ga<sup>3+</sup> in gallosilicate NAT zeolites has been found to affect water content and thermal stability,<sup>13</sup> but also the cation exchange properties through a possible variation in the rigidity of the natrolite chain.<sup>14</sup> Besides, it has been demonstrated that a controlled collapse or atomic disordering of NaA zeolite using a decationization approach allows to control its effective micropore size and thus the molecular sieving properties.<sup>15</sup> Chemical etching used to promote additional mesoporosity in microporous zeolites also revealed the role of pre-existing or induced crystal defects.<sup>16-18</sup> Other post-treatments employing an increase in temperature or pressure modify the short- and long-range order due to transformation to disordered states.<sup>19</sup> However, it is noteworthy that the amorphous oxides formed after compression of zeolites, with shock wave absorption properties like MFI frameworks, can preserve an ordered topology.<sup>20</sup> The adsorption of molecules in the zeolite pores can also lead to variation in the degree of order at the short or long-ranges, and change the mechanical properties of MFI.<sup>21-26</sup>

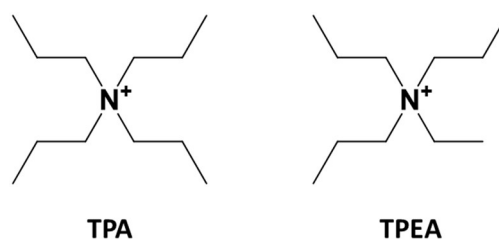
These previous studies, among others, exemplify different types and degrees of disorder and their possible impact on the properties of zeolites. However, the characterization and identification of disorder is usually not a trivial task and there is still a need for a more detailed understanding of the different types of disorder and the possible opportunities to efficiently tune zeolite properties. Most of the examples presented involve the topological specificity of zeolite frameworks and their variations using physico-chemical treatments, during or after zeolite formation. Here, we focus on the MFI

topology and host-guest assemblies involving the related pure silica zeolite (silicalite-1). The MFI topology is described as an assembly of pentasil layers, and has a 3D pore dimensionality made of two types of pore channels along [100] (zig-zag) and [010] (straight) directions, with 10 MR openings. Porous silicalite-1 (after removal of any occluded molecules or ions like structure directing agents) is the most ordered zeolite crystal that can be expected for this topology. It involves only two chemical entities (Si and O atoms), and both crystal and chemical defects (twinning, MEL intergrowth, silanols) can be limited to a minimum. In ambient conditions, its structure is monoclinic with a  $P2_1/n11$  space group and leads to very well resolved powder XRD patterns and  $^{29}\text{Si}$  NMR spectra.<sup>27</sup> By increasing the temperature up to ca. 350 K, a transition occurs towards a more dynamically disordered, although more geometrically symmetric, orthorhombic  $Pnma$  phase.<sup>28-31</sup> It has been noted that an increasing content of  $\text{Al}^{3+}$  leads to a gradual decrease in the temperature of this monoclinic to orthorhombic (m-o) transition.<sup>32</sup> Although the Al site distribution is not random in ZSM-5 zeolites,<sup>33-35</sup> the existence of various possible Al sites is a source of local disorder that increases with Al content as established by multinuclear NMR studies.<sup>36-38</sup> The adsorption of molecules inside the pores of silicalite-1 leads also to a decrease in the m-o transition temperature, and to modifications of the local ordering.<sup>37,39,40</sup> Indeed, the silicalite-1 framework possesses a high flexibility and is strongly impacted by host-guest interactions.

The as-synthesized silicalite-1 zeolites containing an Organic Structure Directing Agent (OSDA) are prototypical examples of host-guest assemblies with MFI topology. To date, the most ordered and defect-free as-synthesized silicalite-1 zeolites are obtained using hydrothermal syntheses with fluoride anions acting as mineralizing agents, and tetrapropylammonium (TPA) as OSDA.<sup>41,42</sup> However, the structure of these well ordered TPA-F silicalite-1 adopts at room temperature the orthorhombic  $Pnma$  phase that can be re-ordered into the monoclinic phase at a low temperature (below ca. 170 K).<sup>43</sup> F atoms are individually located in the  $[4^15^26^2]$  cage exhibiting a rapid exchange between two positions where they bond to a single Si atom.<sup>44-46</sup> This leads to thermal and static disorder in addition to that arising by the motions and conformational states of the TPA. Silicalite-1 zeolites were first formed using TPA and hydroxide anions as mineralizing agents,<sup>47</sup> a synthetic route that promotes a higher content in chemical defects and related disorder. Moreover, other molecules can be used as OSDA, and this opened notably the way to the formation of silicalite-1 and ZSM-5 with lower dimensionality and promising applications in catalysis.<sup>48-50</sup> One interesting feature in these latter systems is the specific positioning of some alkyl groups of the OSDA in the different channels of the MFI topology. For instance, in the case of MFI nano-sheets obtained with amphiphilic diquaternary ammonium (diquats),<sup>48</sup> the hexyl group linking the two nitrogen atoms of the diquat is present in the straight channels. In the case of pillared nano-sheets obtained with symmetric diquats but bearing a shorter pentyl group linker,<sup>49</sup> the models optimized using molecular dynamics showed a higher stabilization energy when the pentyl group is located in the straight channels,<sup>51</sup> a preferential positioning further confirmed by polarized stimulated Raman scattering.<sup>52</sup> A recent study has shown that when a more rigid and bulky linker between the two nitrogen atoms is employed, the newly obtained zeolite retains the straight 10 MR channels along [010] of the MFI

topology but possess a more open and undulated channel along a direction close to [100].<sup>53</sup> Preferential orientations in the MFI channel network have also been noticed when a propyl arm of TPA is replaced by longer or smaller alkyl group.<sup>54</sup> From <sup>13</sup>C NMR analyses, it appeared that butyl arms would be preferentially located at the zig-zag channels, while ethyl arms would be located at the straight channels. These chemical modifications of OSDA are thus influencing the short and long-range ordering in a way that is still to be explored and understood.

In this context, the aim of this work is to decipher the nature of the disorder, and its effects on crystal properties, induced when changing TPA by a slightly less symmetric OSDA in the prototypal host-guest OSDA-silicalite-1 assemblies. We choose to deeply investigate the as-synthesized silicalite-1 obtained using tripropylethylammonium (TPEA, **scheme 1**) due to the novel and intriguing results found. As it will be shown, this highly crystalline host-guest assembly presents a locally correlated geometrical disorder within the zeolite framework and does not show the low *T* m-o phase transition commonly observed for this type of zeolites. We will use point comparisons with OSDA-silicalite-1 assemblies obtained by changing the mineralizing agent (OH<sup>-</sup> vs. F<sup>-</sup>) or the synthesis' method (solvent-free vs. hydrothermal) in order to highlight the specificity of the different kinds of disorder. Long- and short-range organization and ordering will be characterized by a combination of XRD, Raman and multinuclear <sup>13</sup>C, <sup>14</sup>N and <sup>29</sup>Si NMR spectroscopies. The possibility of the low temperature m-o transition will be studied by all these techniques. It will be followed by an analysis of the location of the OSDAs within the host-guest assemblies using refined crystal structures from XRD and complementary <sup>13</sup>C NMR and DFT calculated data. Furthermore, an in-depth study of the as-synthesized crystals by XRD and 2D NMR <sup>29</sup>Si-<sup>29</sup>Si INADEQUATE correlations will allow the description of the local disorder in the zeolite framework. The final discussion will be pointing towards the relationship between the disorder promoted by the hosted OSDA and its implications on crystal properties (e.g. inhibition of the low *T* phase transition). Within this work, we demonstrate how a small modification of the OSDA creates a specific disorder that blocks the phase transition of the organic-inorganic host-guest assembly.



**Scheme 1.** Organic structure directing agents employed.

## RESULTS AND DISCUSSION

### *Preliminary identification of disorder*

The  $^{29}\text{Si}\{^1\text{H}\}$  CP-MAS spectra of four as-synthesized silicalite-1 obtained are presented in **Fig. 1**. When using the hydroxide route (here TPA-OH-HT), it is known that the high degree of chemical connectivity defects (eg.  $\text{SiO}\cdots\text{HOSi}$ ) leads to the identification of less polymerized  $Q^3$  units, and to a wide distribution of environments reflected in the broadening of  $^{29}\text{Si}$  peaks (**Fig. 1A**). The use of fluoride anions as mineralizing agents greatly improves the local ordering.<sup>55, 56</sup> In silicalite-1, F atoms are located inside  $[4^15^26^2]$  cages<sup>44, 46</sup> in rapid exchange between two locations.<sup>45</sup> In these two locations, F atoms are bound to equivalents Si sites (T6 following the numbering of Chao *et al.*, **SI1**)<sup>57</sup> that become five-coordinated units  $[\text{SiO}_4\text{F}]$ . This presence of F prevents almost completely the formation of connectivity defects in the silica framework (FW) with no  $Q^3$  units observed. For long hydrothermal treatments this leads to zeolites (TPA-F-HT) with a high crystallinity and a remarkable resolution in the  $^{29}\text{Si}$  spectra (**Fig. 1B**).<sup>42</sup> However, differences in the width of the  $^{29}\text{Si}$  peaks are still observable depending on the synthesis route. When a faster solvent-free method<sup>58-60</sup> is used (zeolite TPA-F-SF) instead of a long hydrothermal treatment (all reactants being the same), all the peaks are broadened by a factor greater than 2 (**Fig. 1C, SI2**). For this zeolite, transverse relaxation times measured using a spin echo block  $T_2'$  are between 50 and 65 % the values measured for TPA-F-HT (**SI2**). Therefore, the peak broadening cannot be explained solely by this decrease in  $T_2'$ . This broadening comes with a pronounced Gaussian line-shape and is understood as signing distributions of  $^{29}\text{Si}$  chemical shifts  $\delta(^{29}\text{Si})$  for each site as confirmed in the 2D  $^{29}\text{Si}$ - $^{29}\text{Si}\{^1\text{H}\}$  CP-INADEQUATE spectrum described below (**Fig. 10B vs. 10A**). It reveals therefore an increase in the so-called local geometrical disorder due to local variations in the SiO and SiOSi bond distances and angles while keeping an identical topology. Besides, when TPA - the most efficient OSDA for silicalite-1 - is replaced by its analog TPEA (zeolite TPEA-F-HT) in the long hydrothermal synthesis (all the other conditions being preserved), peak displacements are observed (**Fig 1D**), and previously explained by an adaptation of the framework geometry to this slightly smaller OSDA.<sup>54</sup> For TPEA-F-HT we also observe a broadening of the  $^{29}\text{Si}$  peaks (**SI2**), which resembles that of TPA-F-SF. For the same reasons ( $T_2'$  values, Gaussian line-shapes), the peak broadening is related here to a wider distribution in chemical shifts and could be then similarly explained by an increase in the local geometrical disorder.

On the basis of these preliminary results we establish a rough scale in the degree of local disorder for the four types of as-synthesized zeolites. The hydroxide route leads to the highest disorder (chemical and geometrical) on the contrary to the fluoride route, and modifications in this fluoride route (OSDA, synthesis' protocol) introduce some degree of geometrical disorder, yielding: TPA-OH-HT > TPA-F-SF  $\approx$  TPEA-F-HT > TPA-F-HT. But this scale can mask drastic differences in the nature of the geometrical disorder that would be of interest to further characterize.

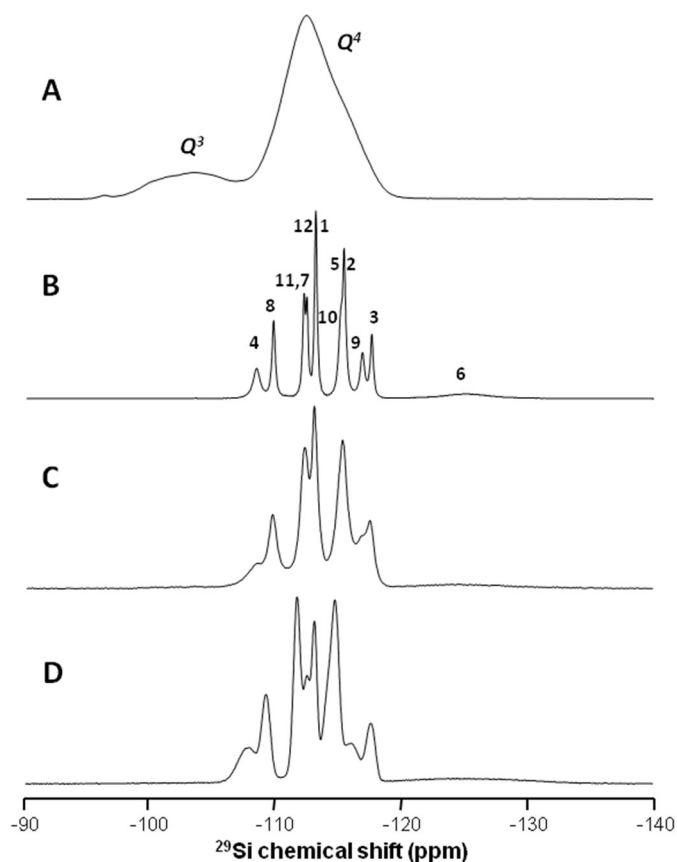


**Fig. 1.** 1D  $^{29}\text{Si}\{^1\text{H}\}$  CP-MAS spectra ( $\nu_0[^{29}\text{Si}] = 79.5$  MHz,  $\nu_{\text{MAS}} = 5$  kHz) of as-synthesized zeolites: (A) TPA-OH-HT, (B) TPA-F-HT, (C) TPA-F-SF, (D) TPEA-F-HT. The assignment of the  $^{29}\text{Si}$  peaks in (B) is obtained combining previous crystallographic<sup>57</sup> and NMR data<sup>46</sup> with data obtained on our samples (see text for more details).

### ***Contrasted low temperature behaviors***

*XRPD.* Highly crystalline TPA-F-HT was studied by x-ray powder diffraction as a function of temperature. As in previous work,<sup>43</sup> strong splitting of many reflections occurs below 175 K due to the transition to the monoclinic phase (**Fig 2A**). The diffraction lines that split are broadened due to the strain induced by the formation of ferroelastic twin domains.<sup>31</sup> In the present work, Le Bail refinements were performed to obtain the unit cell parameters and volume (**Table 1**). The thermal contraction of the material is very small with essentially continuous decreases in the unit cell parameters upon cooling (**Fig 2B-C**). This is distinct from the behavior of calcined silicalite-1, which is complex and for which negative volume thermal expansion occurs over a certain temperature range linked to the absence of guest molecules in the pores.<sup>61</sup> The  $\alpha$  angle of TPA-F-HT strongly increases at the phase transition and reaches 90.581(1) at 20 K. This is very similar to the value for monoclinic calcined silicalite-1 at room temperature.<sup>31</sup>

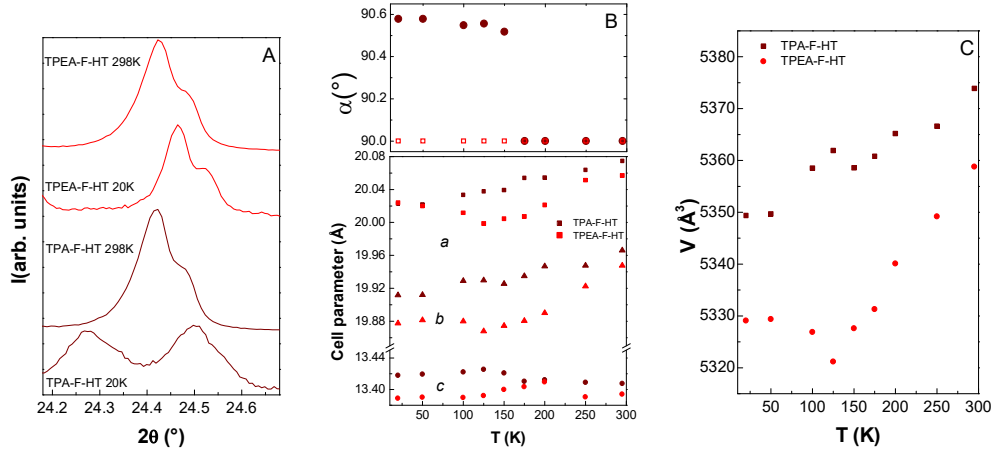


**Fig. 2.** Comparison of X-ray ( $\text{Cu K}\alpha_1$  et  $\text{K}\alpha_2$ ) powder diffraction data of TPA-F-HT and TPEA-F-HT zeolites. (A) XRD patterns in the region of the 313 orthorhombic reflection. (B) Unit cell parameters, angle  $\alpha$  and (C) volume as a function of temperature. Standard uncertainties are smaller than symbol sizes.

**Table 1.** Unit cell parameters of as-synthesized silicalite-1 materials at low and room temperatures.

Material	$T(\text{K})$	Crystal system	$a(\text{\AA})$	$b(\text{\AA})$	$c(\text{\AA})$	$\alpha(^{\circ})$	$V(\text{\AA}^3)$
TPA-F-HT	298	Orthorhombic	20.0746(1)	19.9661(1)	13.4075(1)	90	5373.85(6)
TPA-F-HT	20	Monoclinic	20.0221(5)	19.9116(6)	13.4182(3)	90.581(1)	5349.2(2)
TPA-F-SF	298	Orthorhombic	20.0701(3)	19.9679(3)	13.4069(2)	90	5372.9(1)
TPA-F-SF	50	Monoclinic	20.0331(4)	19.9333(4)	13.4129(3)	90.462(1)	5355.9(2)
TPA-OH-HT	298	Orthorhombic	20.0540(5)	19.9473(6)	13.4160(4)	90	5366.7(3)
TPA-OH-HT	50	Orthorhombic	20.0512(5)	19.9300(5)	13.4077(4)	90	5358.0(3)
TPEA-F-HT	298	Orthorhombic	20.0570(1)	19.9476(1)	13.3940(1)	90	5358.79(5)
TPEA-F-HT	20	Orthorhombic	20.0277(5)	19.8645(5)	13.3903(3)	90	5327.2(2)

The presence of disorder in as-synthesized silicalite-1 made with TPA modifies the phase transition behavior at low temperature (**Fig. 3**). In TPA-F-SF, which exhibits a moderate degree of disorder, the transition occurs at essentially the same temperature, but the monoclinic angle increases at a much slower rate and is more than  $0.1^{\circ}$  smaller than in TPA-F-HT at low temperature. In the case of the TPA-OH-HT prepared by the hydroxide route and presenting a high degree of chemical and geometrical disorder, the transition is not observed and the material remains orthorhombic at least down to 50 K. The results indicate that, as in calcined silicalite-1, disorder can decrease the phase transition temperature and even potentially suppress the transition.

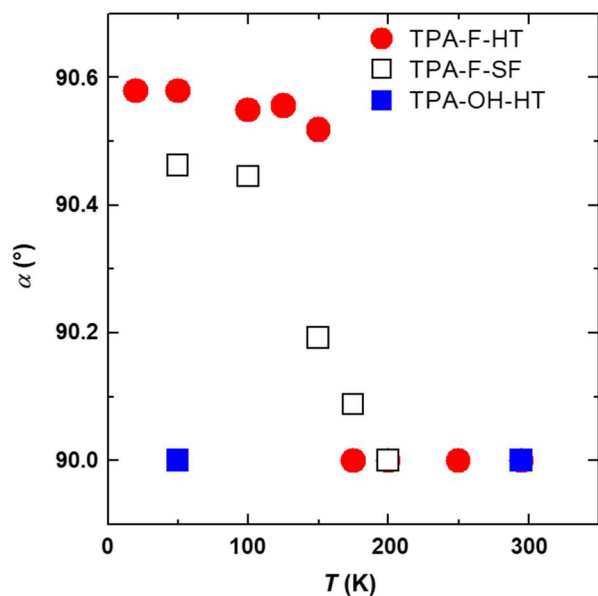


**Fig. 3.** Monoclinic angle of TPA-silicalite-1 assemblies as a function of temperature.

The case of TPEA-F-HT that is highly crystalline (**SI3**) and exhibits a moderate degree of geometrical disorder at a local level is intriguing. This material with a slightly smaller OSDA has systematically lower cell parameters and volumes and remains orthorhombic down to 20 K with very sharp diffraction lines (**Fig. 2**). This indicates that only a very small modification of the OSDA with only one CH<sub>2</sub> unit less in one chain modifies the unit cell volume, completely suppresses the phase transition and stabilizes the high  $T$  orthorhombic form down to 20 K. The orientational disorder in the lower symmetry OSDA can be evocated to explain the stabilization of the paraelastic phase at low  $T$ . In the following, we will focus in these differences induced by the OSDA.

*Raman.* Low temperature Raman investigations were performed on single crystals of TPA-F-HT and TPEA-F-HT down to 10 K (**Fig. 4**). The changes observed for the two host-guest zeolites are presented in three spectral regions: 125-600 cm<sup>-1</sup> (principally Si-O-Si bending), 600-1600 cm<sup>-1</sup> (Si-O, C-C, C-N stretching, H-C-H bending, wagging, rocking) and 2700-3100 cm<sup>-1</sup> (C-H stretching).

**Table 2.** Raman data (cm<sup>-1</sup>) of TPA-F-HT and TPEA-F-HT at the selected temperatures.

TPA-F-HT 10K	TPA-F-HT 300K	TPEA-F-HT 10K	TPEA-F-HT 300K	intensity	Assignment <sup>62-65</sup>
3027					
3022	3020	3020		w	
3012		3015	3011	w	
3001					
2992	2991	2990	2991	s	$v_{as}$ CH <sub>3</sub>
2987					
2980			2979		
2975	2977	2974			$v_{as}$ CH <sub>3</sub>
2968		2966	2965		
2962	2956	2951	2954		$v_{as}$ CH <sub>2</sub>

2944	2944	2940	2942	s	v <sub>s</sub> CH <sub>3</sub>
2933		2930			
2921	2924	2922	2923	m	v <sub>s</sub> CH <sub>2</sub>
2911	2905	2914			v <sub>s</sub> CH <sub>2</sub>
		2901	2902		
2893	2895	2892	2894	m	
2888	2890	2888	2890	s	v <sub>s</sub> C-H <sub>2</sub>
2754	2755	2753	2754		overtone CH <sub>3</sub>
1460	1460	1463	1461	vs	δ CH <sub>2</sub>
1357	1357	1356	1358	m	
1348	1345		1349	w	ω CH <sub>2</sub>
1341		1341	1340		ω CH <sub>2</sub>
1333	1333	1335		m	ω CH <sub>2</sub>
1323	1319	1321	1322	w	ω CH <sub>2</sub>
		1312		m	ω CH <sub>2</sub>
1197				vw	
1186	1186			w	
1180		1180		m	
1172	1172		1175	m	ρ CH <sub>2</sub>
1157		1157	1154	w	ρ CH <sub>2</sub>
1147	1145	1141	1141	m	ρ CH <sub>2</sub>
1116				m	v C-C
1106	1104	1104	1104	s	v <sub>as</sub> C-C
		1090	1088	s	
1048				s	v <sub>as</sub> C-N
1042	1043	1043	1043	s	v <sub>as</sub> C-N
1036	1034	1035	1035	ms	v C-C
		1024			v <sub>s</sub> C-N
993	990				
982		982		w	
971	976		978		ρ CH <sub>3</sub>
		962	961	w	v <sub>s</sub> C-N
		952		w	
939	937				v <sub>s</sub> C-N
925	922	928	928	m	
919		915	914	s	v <sub>s</sub> C-N
901	904				
890	894	889	892	m	
873	870	869	872	m	
863					
851	848	846		m	ρ CH <sub>3</sub>
838	835	839	839	m	v <sub>s</sub> Si-O 5MR
818	808		813	w	v <sub>s</sub> Si-O 4MR
803	790	802	798	w	v <sub>as</sub> Si-O 6,10MR
779	773	764		m	v <sub>s</sub> C-N
756			760	w	
749	752	751	752		v <sub>s</sub> C-N
		733	733	s	v <sub>s</sub> C-N
	596	595			δ Si-O-Si
580	585	581	584		δ Si-O-Si
567	576		565		
554	551				
541	537	541	539		δ Si-O-Si
517	516	518	517		δ Si-O-Si
		490			
		469	471		δ Si-O-Si 4MR
459	451	457	454		

437	434	436	435	
424		421		$\delta$ Si-O-Si
395		395		
385	385	385	386	$\delta$ Si-O-Si 5MR
		376		$\delta$ Si-O-Si
372	367	369	369	
361		361		$\delta$ Si-O-Si 6MR
341	343	346	343	
		336		
323	328	314		
310	307	307	312	OSDA def.
296	292	294	291	$\delta$ Si-O-Si 10MR
282				
275		275		
262	267	265	268	
251				
237		233		
222				
213		217		
201				translation of Si/Si lattice modes,
197		197		rotation of the fragment of zeolite chain
190				
187		186		
178		179		
175		173		
171				
161				
158		156		

In the low wavenumber region, Si-O-Si bending of the MFI framework, the spectra of TPA-F-HT and TPEA-F-HT are very similar over the 180-300 K temperature range. Some modes are found in slightly different positions, for example 307  $\text{cm}^{-1}$  in TPA-F-HT versus 312  $\text{cm}^{-1}$  in TPEA-F-HT, which is in fact a low wavenumber mode of the OSDA, and an additional mode observed at 471  $\text{cm}^{-1}$  for TPEA-F-HT (**Table 2**). In the case of TPA-F-HT, a major change occurs between 180 and 170 K. At 170 K and below, modes that were previously overlapped become clearly separated, in particular the modes linked to the 5 MR and 6 MR at 385-395  $\text{cm}^{-1}$  and 361-376  $\text{cm}^{-1}$ , respectively. Due to this separation, small shifts in the peak maxima can be observed. These peaks become very sharp between 150 and 125 K and only minor further changes are observed down to 10 K. The principal change thus occurs at the m-o phase transition temperature due to modifications to the geometry of the 5 MR, 6 MR and 10 MR. Based on group theory, no additional Raman modes are expected for the monoclinic phase as all the gerade modes are active for both symmetries. Many peaks are observed in the region below 290  $\text{cm}^{-1}$  corresponding to further Si-O-Si bending modes and lattice modes. These modes have previously been observed in Raman spectra of monoclinic calcined MFI samples at room temperature.<sup>65</sup> They correspond to broad features in the spectra of orthorhombic form indicating an increase in order in the monoclinic form. In contrast for TPEA-F-HT, a different behavior is observed. Changes occur between 170 and 160 K. In the region of the Si-O-Si bending modes of the 5 MR and 6 MR a broad series of overlapping peaks with modified intensities is observed down to 10 K, indicating that a large number of geometrical

configurations are present corresponding to the existence of static geometrical disorder. The splitting of bending modes near  $270\text{ cm}^{-1}$  is observed at the lowest temperatures. Finally, in the region below  $250\text{ cm}^{-1}$ , the lattice modes are much broader in TPEA-F-HT due to the presence of static disorder corresponding to a vibrational density of states.

In the  $600\text{-}1600\text{ cm}^{-1}$  range, where Si-O, C-C, C-N stretching, H-C-H bending, wagging, and rocking are observed, some clear differences exist between TPEA-F-HT and TPA-F-HT, there are more modes in TPEA due to presence of the ethyl and the propyl groups. Strong additional peaks at  $733\text{ cm}^{-1}$  and  $1088\text{ cm}^{-1}$  are observed in the C-N stretching and  $\text{CH}_2$  rocking regions for TPEA-F-HT, which could be characteristic of the ethyl group. Upon decreasing temperature, the modes of both materials gradually sharpen and some splitting is observed. The changes do not occur at a specific temperature, such as the m-o phase transition temperature, indicating these internal modes of the OSDA and the  $\text{SiO}_4$  tetrahedra are insensitive to the changes occurring at long range.

In the  $2700\text{-}3100\text{ cm}^{-1}$  C-H stretching region, the spectra of TPEA-F-HT and TPA-F-HT are very similar with the exception of an additional peak at  $2965\text{ cm}^{-1}$  in TPEA-F-HT at ambient temperature. In TPEA-F-HT, slight gradual changes occur upon cooling to 10 K with the vibrational bands remaining broad even at low temperature consistent with the freezing in of the disorder present in this material. In the case of TPA-F-HT, gradual changes also occur with no abrupt discontinuity at the phase transition. However, the bands continue to sharpen below 100 K and a strong splitting is present at 10 K. This is consistent with a much more ordered state, corresponding to a correlated reduction in the motion of the propyl arms. In addition, some C-H modes have lower wavenumber values at low  $T$  indicating a weakening of the C-H bonds due to increased long-range interactions such as weak CH...O hydrogen bonds.<sup>66</sup> This process is favored by the reduced motion of the alkyl groups.

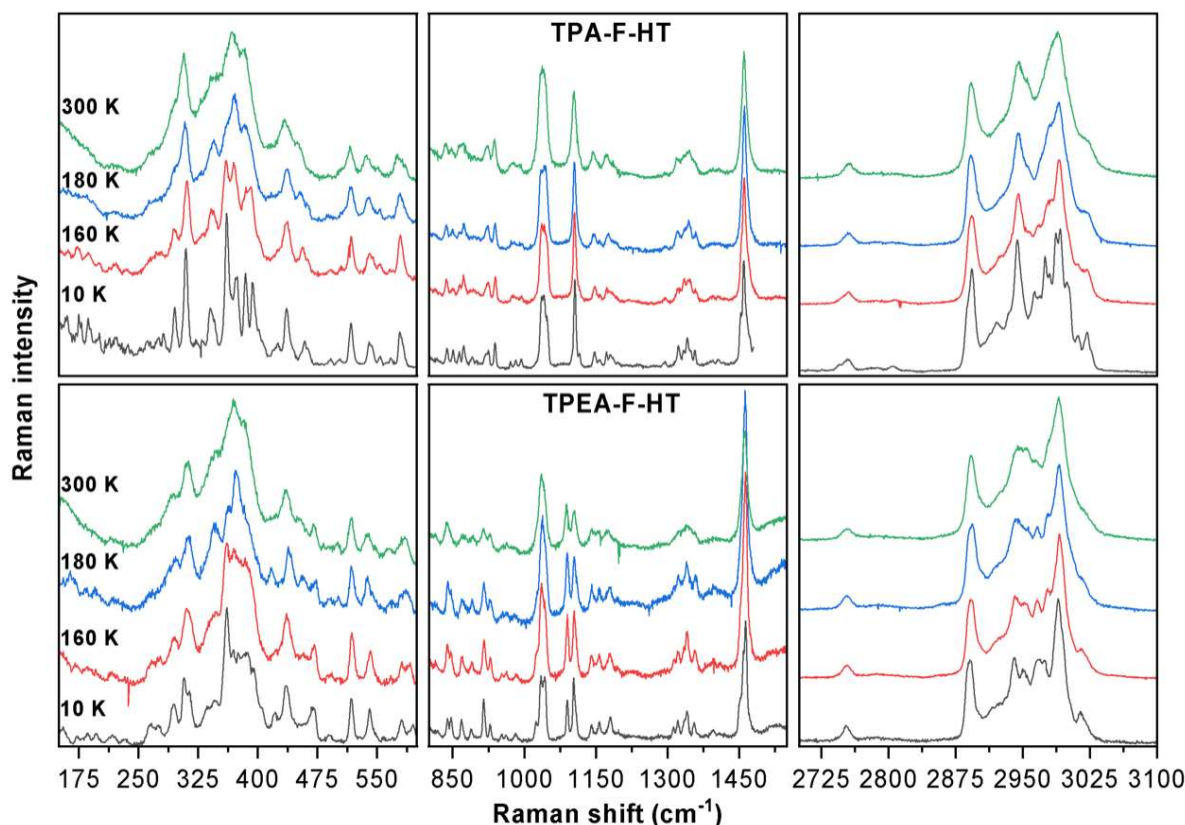


Fig. 4. Selected Raman spectra of TPA-F-HT and TPEA-F-HT as a function of temperature.

$^{29}\text{Si}$  NMR. In the case of TPA-F-HT, the variations of  $^{29}\text{Si}\{^1\text{H}\}$  CP-MAS spectra as a function of  $T$  confirm previously published data (Fig. 5A).<sup>45</sup> At room temperature, the spectrum presents the resonances of the 12 Si sites of the  $Pnma$  phase including the broad peak at ca. -125 ppm related to the two crystallographic equivalent T6 sites in the fast exchange regime due to the jumps of the F atoms between these sites inside  $[4^15^26^2]$  cages (*vide supra*). At low  $T$ , before the m-o transition, this peak splits into two lines characteristic of the  $[\text{SiO}_4]$  unit and the penta-coordinated  $[\text{SiO}_4\text{F}]$  unit involved in the dynamic exchange process. This evolution is consistent with that previously obtained and allows to describe the exchange dynamics (see S14). When the m-o transition occurs the F exchange rate constant is estimated here to ca.  $3500\text{ s}^{-1}$ . Below the transition temperature, very narrow peaks ( $T_2^*$  between 5 and 15 ms) are recorded for the monoclinic structure. An unambiguous spectrum deconvolution with 17 different separated peaks (among the 24 expected resonances) is obtained by fitting.

In the case of TPEA-F-HT, the  $^{29}\text{Si}$  spectra follow a similar evolution when decreasing  $T$ , but with broader peaks (Fig. 5B). For instance, the slowdown of the F exchange also leads to a peak splitting. At temperatures below the m-o transition observed for TPA-F-HT, the peaks stay broadened compared to the TPA zeolite, but they are located at similar chemical shifts (see S15).  $T$  gradients inside the sample could not explain the observations here made since the  $^{29}\text{Si}$  spectra recorded for each zeolite at the temperatures of 151 and 133 K are very similar.

By spectrum fitting, a weighted average of the  $^{29}\text{Si}$  chemical shifts is estimated for each spectrum. For both zeolites, this semi-quantitative parameter shows a decrease with temperature (see **SI6**) that can be related to the decrease in Si-O-Si angles observed in the crystal structures. A gap for this parameter, and for both zeolites, is observed in the temperature range related to the crystallographic transition of TPA-F-HT.

From this  $^{29}\text{Si}$  NMR study, we conclude that the same type of variations in local geometry (Si-O-Si angles) and dynamics (F exchange) occur for both as-synthesized zeolites when decreasing the temperature. The broadening of the peaks observed at 188 K can be understood by local and preliminary geometrical variations of the structure that lead to a collective phase transition in one case, and that remains blocked in the other case. The use of TPEA leads to broader  $^{29}\text{Si}$  peaks in the complete  $T$  range explored. This additional peak broadening in TPEA-F-HT can be related to a larger static distribution in the Si environments promoted by the lower symmetry of the OSDA which is a possible explanation for the blocked m-o transition.

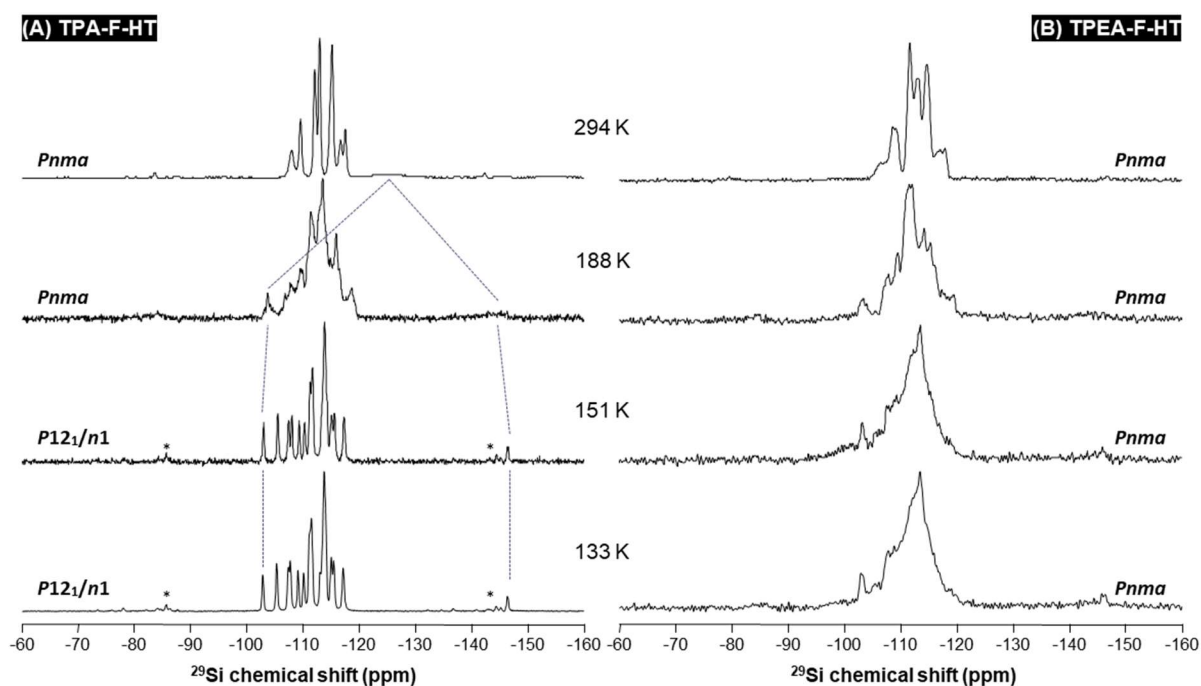


**Fig. 5.**  $^{29}\text{Si}\{^1\text{H}\}$  CP-MAS spectra of TPA- and TPEA-F-HT zeolites recorded at different temperatures ( $\nu_0[^{29}\text{Si}] = 119.2$  MHz,  $\nu_{\text{MAS}} = 3.5$  kHz). The dashed lines highlight the splitting of the  $^{29}\text{Si}$  peak located at ca. -125 ppm related to the evolution of the chemical exchange regime (fast to slow at low  $T$ , see text). The asterisks show the spinning sidebands.

$^{13}\text{C}$  NMR. Information on the variations in OSDA conformations and ordering can be inferred from  $^{13}\text{C}$  NMR spectroscopy. At ambient temperature, the typical  $^{13}\text{C}\{^1\text{H}\}$  CP-MAS spectrum of TPA-F-HT (**Fig. 6A**) presents two peaks in a 1:3 ratio for the methylene carbons bound to nitrogen  $\text{C}_\alpha(\text{Pr})$ , a composite peak for the methylene carbons in the middle of the propyl arm  $\text{C}_\beta(\text{Pr})$ , and two peaks in a 1:1 ratio for

the methyl groups  $C_{\alpha}(\text{Pr})$ .<sup>42</sup> These latter peaks at ca. 11 and 10 ppm have been assigned respectively to methyl groups in the straight and the sinusoidal MFI pore channels using experimental NMR data,<sup>67</sup> in agreement with further calculated dynamics using a cluster approach.<sup>66</sup> When one propyl arm is replaced by an ethyl arm as in TPEA-F-HT, the peak at 11 ppm decreases roughly by a factor two, while the peak at 10 ppm keeps its initial relative intensity (**Fig. 6B**). This effect has been explained by the preferential location of ethyl arms in the MFI straight channels.<sup>54</sup> For this zeolite, we can also notice the presence of three peaks for  $C_{\alpha}(\text{Pr})$  related to slightly different time-averaged conformational states for the three propyl arms.

When decreasing the temperature from 294 to 188 K, just before the transition to the monoclinic phase for TPA-F-HT, a systematic broadening is observed for all peaks. Following a previous  $^{13}\text{C}$  NMR study on this zeolite,<sup>68</sup> this broadening would account for a decrease in the mobility of the OSDA. The spectra recorded here for TPEA-F-HT in the 294-188 K range show a similar trend although no phase transition is observed. In addition to motional changes, the broadening would be explained more reasonably assuming a disorder promoted by the geometrical variations of the structure inferred from the  $^{29}\text{Si}$  NMR analysis (*vide supra*).

As expected, the  $^{13}\text{C}$  CP-MAS spectra recorded at 133 K present several distinguishable peaks for TPA-F-HT (14 over a maximum of 16), related to the specific conformational states of each propyl arm in the less symmetric monoclinic phase. Interestingly, this is not the case for TPEA-F-HT, its  $^{13}\text{C}$  spectrum being almost equivalent to that recorded at 188 K. Over the total  $T$  range, no new  $^{13}\text{C}$  peaks are observed for this zeolite, and the variations solely concern the broadening and shift of the resonances (see **SI7**). For TPEA-F-HT, we thus observe the stable positioning of the ethyl arms in the straight channels at all  $T$ , and the absence of conformational changes at low  $T$  in the range where TPA-F-HT presents drastic changes.

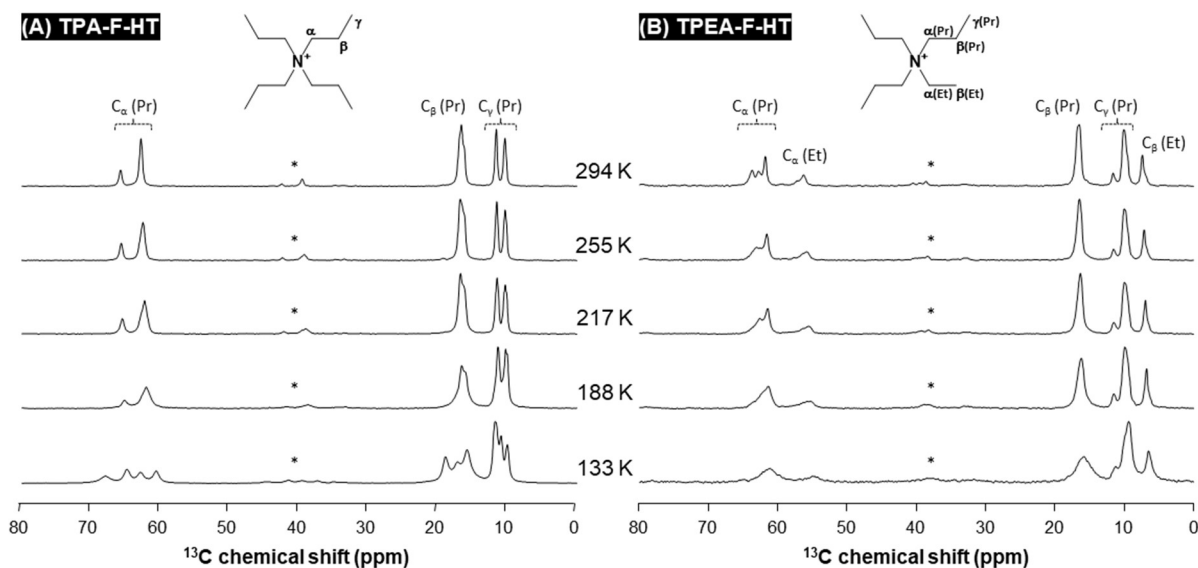


**Fig. 6.**  $^{13}\text{C}\{^1\text{H}\}$  CP-MAS spectra of TPA- and TPEA-F-HT zeolites recorded at different temperatures ( $\nu_0[^{13}\text{C}] = 150.8$  MHz,  $\nu_{MAS} = 3.5$  kHz). Asterisks refer to spinning sidebands' peaks.

$^{14}\text{N}$  NMR. The local order and dynamics at the OSDA sites in as-synthesized zeolites can be inspected by  $^{14}\text{N}$  NMR spectroscopy.<sup>69-71</sup> The  $^{14}\text{N}$  spectra recorded at room  $T$  agree with the previous results obtained for the two OSDA (TPA, TPEA) with a spinning sidebands (SSB) pattern dominated by the quadrupolar coupling interaction ( $C_Q = 53$  kHz).<sup>54,69</sup> For both TPA-F-HT and TPEA-F-HT the evolution of the  $^{14}\text{N}$  SSBs is the same in the temperature range well above the m-o transition (here 217-294 K). When decreasing  $T$ , we observe a slight increase in the quadrupole coupling constant  $C_Q$  up to 60 kHz and a broadening of the observed peaks (**Fig. 7**). For instance, the apparent transverse relaxation time  $T_2^*$  decreases from 8.6 ms down to 1.3 ms for TPA-F-HT. At 188 K, the signals become hard to detect due to a severe broadening of the peaks. Around the  $T$  range of the m-o transition (185-150 K), no signal could be recorded for both as-synthesized zeolites. When further decreasing the temperature (133 K), a low  $T$  spectrum is obtained for TPA-F-HT thanks to a peak narrowing ( $T_2^*$  increases up to 0.5 ms). In this case, the SSB pattern widens presenting a  $C_Q = 108$  kHz larger than that measured at RT. However, it is still not possible to record a proper  $^{14}\text{N}$  NMR signal for TPEA,  $T_2^*$  values remain probably too small.

These evolutions in the experimental  $^{14}\text{N}$  NMR spectra of TPA-F-HT bear a high similarity with the theoretical studies of transitions between two different motional states.<sup>72</sup> There is a minimum in  $T_2$  at the transition point, and different apparent  $C_Q$  values are observed above and below the transition. Moreover, the  $C_Q$  values measured above the m-o transitions are close to those calculated from dynamic simulations<sup>66</sup> while those measured at 133 K approach the  $C_Q$  values calculated for model structures optimized without considering dynamics.<sup>66,73</sup> We therefore conclude that the m-o transition is accompanied by a transition in the TPA's motional regimes, and we hypothesize that the degree of motions of the OSDA are more restrained in the monoclinic phase. This is in line with previous studies on TPA motions through  $^1\text{H}$  and  $^{13}\text{C}$  NMR experiments.<sup>68,74</sup> These early works concluded on the

presence of a complex combination of librations of propyl arms and oscillations of the whole cation above the m-o transition, that are greatly attenuated below the transition. Such differences in motions can here explain the  $^{14}\text{N}$  variations in  $C_Q$  and  $T_2$  observed for TPA-F-HT. It is also accompanied by a transition in the conformational changes as observed by  $^{13}\text{C}$  NMR (*vide supra*). Interestingly this transition in the motional regimes cannot be observed for the TPEA-F-HT zeolite that appears again to stay blocked in an intermediate and more disordered state when decreasing  $T$ .

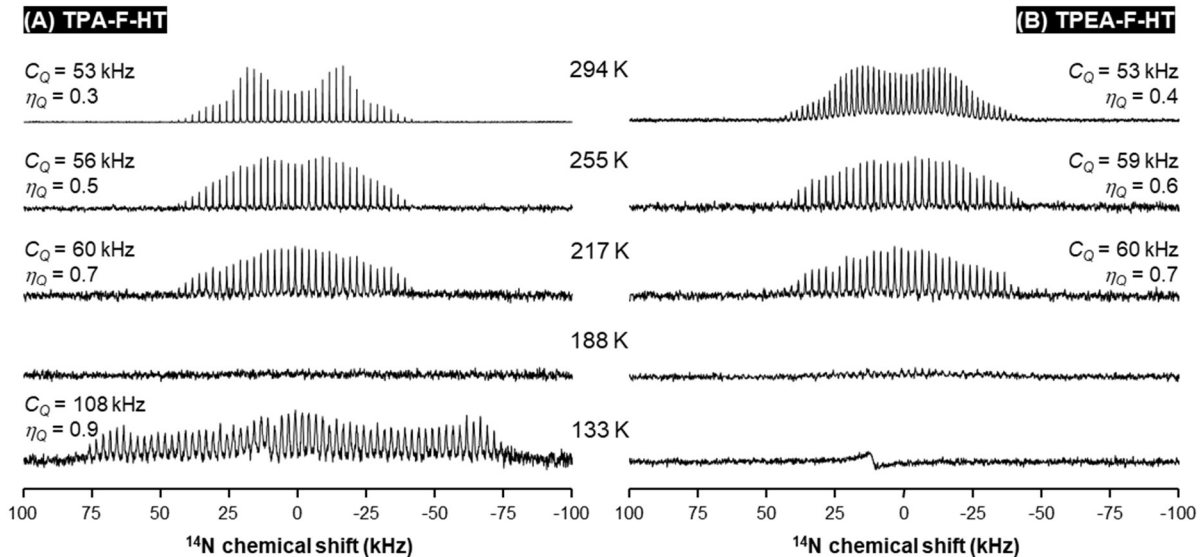


**Fig. 7.**  $^{14}\text{N}$  spinning sidebands patterns of TPA- and TPEA-F-HT zeolites recorded at different temperatures ( $\nu_0[^{14}\text{N}] = 43.3$  MHz,  $\nu_{MAS} = 2.5$  kHz, except TPEA-F-HT at 294 K for which  $\nu_{MAS} = 2.0$  kHz). Quadrupolar coupling parameters ( $C_Q$ ,  $\eta_Q$ ) are estimated by spectrum fitting.

### ***OSDA location in the silicalite-1 host***

In order to discuss further the local disorder related to the OSDAs, it appears necessary to position these OSDAs with respect to the silica framework. Experimental structures of as-synthesized silicalite-1 at room temperature have been previously determined by x-ray diffraction for crystals synthesized with TPA in a hydroxide,<sup>75,76</sup> and in a fluoride medium.<sup>44,77,78</sup> The structures are metrically pseudo-tetragonal, but the actual atomic structure is orthorhombic, space group  $Pnma$ , where crystals are usually pseudo-merohedrally twinned by a two-fold rotation axis along the  $a+b$  diagonal. Aubert *et al.* explicitly mentioned this twinning with refined twin volume fractions of 0.4770(9), whereas van Koningsveld *et al.* probably have not considered twinning. Aubert *et al.* also considered the non-centrosymmetric subgroup  $Pn2_1a$  but found no evidence for a more accurate description of the structure than in the centrosymmetric parent space group. We focus here on the structures of TPA-F-HT and TPEA-F-HT obtained at  $T = 100$  K, a temperature that allows to freeze some of the OSDA motions and to obtain a more detailed structural information. **Fig. 8** presents schematically the location and orientation of the propyl arms of TPA (A1-A4) in silicalite-1 structures considering the most common

space groups  $Pnma$  and  $Pn2_1a$  envisaged for the orthorhombic phase. In the case of  $Pnma$  the mirror planes normal to the  $b$  axis impose an equivalency between two propyl arms located in the straight channels, otherwise absent in the case of  $Pn2_1a$ .

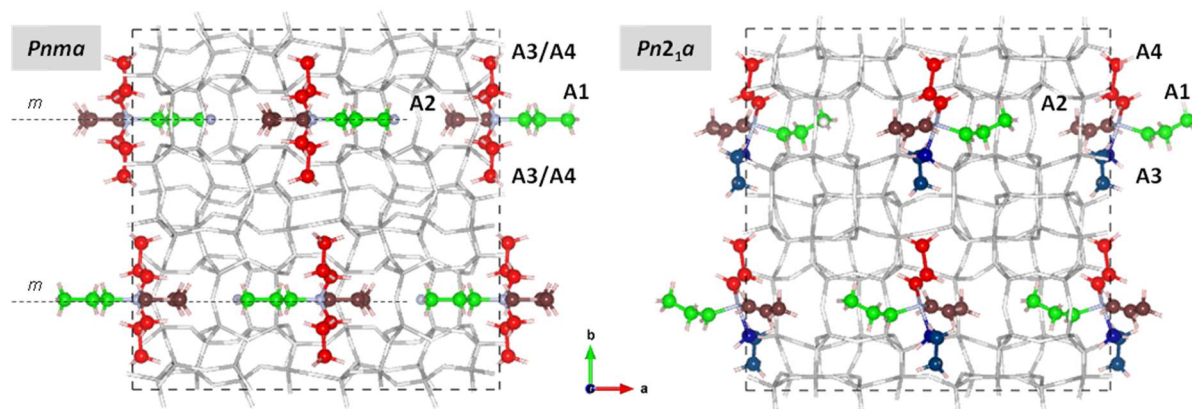


**Fig. 8.** Location and orientation of propyl arms of TPA (A1-A4) inside the unit cells of the orthorhombic structures  $Pnma$  and  $Pn2_1a$  (projection onto the  $ab$  plane). The C atoms of the unequivalent arms are represented in different colors. Si, O, F and H atoms are omitted for the sake of clarity, bonds are represented as sticks.

**TPA-F-HT at 100 K.** The structural model of TPA obtained after refinement is presented in **Fig. 9A**. It shows that there is still unresolved disorder, because of the misalignment of a couple of thermal ellipsoid axes between neighboring carbon atoms. It is noted that no attempt was made to artificially line up these axes by using so-called DELU restraints meaning that the components of the anisotropic displacement parameters in the direction of the bond are kept approximately equal during the refinement. There is a considerable scatter in the tetrahedral angles around the central nitrogen atom,  $96(2)^\circ$ - $126(1)^\circ$  (standard deviation:  $12.7^\circ$ ). This range about the ideal tetrahedral angle of  $109.5^\circ$  - not considered to be as a real deficiency of the model - can explain the spreading of  $^{13}\text{C}$  NMR chemical shifts for  $\text{C}_\alpha$  observed at low  $T$  (**Fig. 6A**). In addition, the deviations from  $T_d$  symmetry at the N sites are known to lead to higher  $C_Q(^{14}\text{N})$  values for tetraalkylammonium cations<sup>79</sup> as also observed here at low  $T$ . The internal alkyl angles have a much more skewed distribution between  $112(1)$  and  $128(2)^\circ$ , which is probably due to not taking into account the unresolved disorder. Also to note the orientation of the C4-C5-C6 arm in monoclinic TPA-F-HT seems to be distinctively different from that in orthorhombic TPEA-F-HT (**Fig. 9 B-C**).

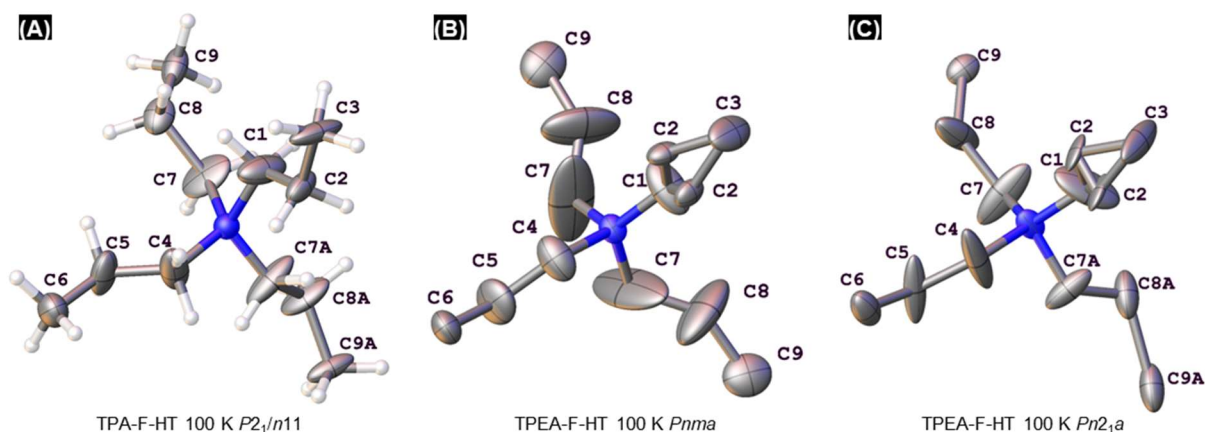


**Fig. 9.** Structural models of OSDA in: TPA-F-HT with space group  $P2_1/n11$  (A), TPEA-F-HT with space groups  $Pnma$  (B) and  $Pn2_1a$  (C). Atomic displacement ellipsoids are at the 25% probability level. In the case TPEA-F-HT (A, B), it is not possible to localize the ethyl arm along a single direction but rather in the two possible directions parallel to the  $b$  axis related to  $C7/C7A$ ,  $C8/C8A$  and  $C9/C9A$  (see text for detail). Note that the view directions in A, B and C are:  $-a^*+1.548b^*-21.105c^*$ .

**TPEA-F-HT at 100 K.** Refinements were carried out in the  $Pnma$  and  $Pn2_1a$  space groups. The model was gradually built using successive difference Fourier syntheses. Rather than developing a sophisticated disorder model using many additional constraints, it was decided to let the anisotropic displacement parameters freely float for the individual atoms in the molecule. In this way, the disordered regions are easily visualized without biasing the refinement to a desired structural model. Very anisotropic and large displacement ellipsoids can be the sign of either static or dynamic disorder. Restraints were only used for the C-C intramolecular bond distances (1.50(2) Å), but angles were allowed to freely refine. The only constraint used was a common occupancy factor for the complete molecule. One carbon position (C2) was clearly split in two sites that were used in the refinement with half occupancies compared to the overall occupancy of the molecule. In space group  $Pnma$  there are three independent alkyl arms: C1-C2-C3 (A1), C4-C5-C6 (A2), and C7-C8-C9 (A3) of which the first two lie in the mirror plane perpendicular to the  $b$ -axis (**Fig. 8**). The mirror image of the third arm, A4, completes the TPEA molecule. In space group  $Pn2_1a$  the four arms are crystallographically independent. **Fig. 9** gives a view of these models in  $Pnma$  (**9B**) and  $Pn2_1a$  (**9C**) which shows in the first place that the tetrahedral  $sp^3$  angles within the alkyl chains are reasonably well preserved although they were not restrained. The overall occupancy of the TPEA molecule site is 0.847(17) for  $Pnma$  and 0.94(2) for  $Pn2_1a$ , whereas the occupancies of the two fluorine sites are 0.40(1) and 0.42(1) for  $Pnma$  and  $Pn2_1a$ , respectively, which corresponds to 0.80 and 0.82 fluorine atoms per unit cell. It should be noted that the refinements in  $Pnma$  are completely stable, but that the presence of the pseudo-mirror in  $Pn2_1a$  is a source of bad convergence of the refinement and high correlations between several parts of the siloxane matrix. The more stable model in  $Pnma$  shows that the disorder in the C7-C8-C9 arms is probably of a different nature and larger than in the arms on the mirror plane.

In order to assess which arm positioned in these structures contains the ethyl group, the occupancies of the different arms were refined individually, but this time with imposed similarity restraints on the atomic displacement parameters (SIMU and DELU *SHELXL*<sup>80</sup> instructions). The refined occupancies in this way in the *Pnma* model are 0.85(3), 0.75(3), and 0.67(3) for A1, A2, and A3, respectively. This suggests that A3 has the highest probability to contain the ethyl group. The same refinement strategy with some tighter restraints on the atomic displacement ellipsoids for the model in *Pn2<sub>1</sub>a* gave basically the same results with refined occupancies of 0.94(3), 0.85(3), 0.72(3), and 0.65(3) for arms A1, A2, A3, and A4, respectively. Although it seems clear now also from XRD that the ethyl chains are located within the channels perpendicular to the mirror plane, i.e. within the straight channels, no clear distinction can be made between the models in *Pnma* and *Pn2<sub>1</sub>a*, so that a disordered model in the higher symmetry space group should be privileged. Besides, the small differences between the occupancy of A3 and A4 arms in *Pn2<sub>1</sub>a* does not allow to discriminate between a preferential direction taken by the ethyl groups in the straight channels among the two possible. This undifferentiation between directions is an additional source of disorder that can explain the higher anisotropy of displacement observed in *Pnma* and *Pn2<sub>1</sub>a* for carbons C7 and C7A, and for nitrogen (**Fig. 9 B-C**) compared to TPA-F-HT (**Fig. 9A**).

From the comparison of <sup>13</sup>C NMR data for TPA and TPEA containing silicalite-1 zeolites, and notably for the latter from the ~50 % decrease in amplitude of the <sup>13</sup>C peak related to methyl groups of the propyl arms inside the straight channels along the [010] direction, it was concluded that ethyl arms are mainly present in these straight channels.<sup>54</sup> Our new <sup>13</sup>C{<sup>1</sup>H} CP-MAS spectra confirm this view (**Fig. 6** and **SI8**). The observation of three different peaks for C<sub>α</sub>(Pr) in TPEA-F-HT, and one for C<sub>α</sub>(Et), indicates that there are different conformational states for each propyl arm, and possibly one main location for the ethyl arm (in one direction of the straight channel). However, the higher spectral resolution of the new spectra allows to observe additional small peaks, notably for C<sub>β</sub>(Et), suggesting that there is not a single environment for the ethyl arms. This could be explained by the four possible locations of the ethyl arms, the two in the straight channels being the most probable.

Otherwise, the presence of ethyl arms in the straight channels leads in principle to a break in the highest crystal symmetry usually considered for as-synthesized silicalite-1. If this occurs in an ordered manner, there cannot be a mirror plane normal to (010) planes anymore, and the space group has to be changed, for instance from *Pnma* to *Pn2<sub>1</sub>a* (**Fig. 8**). We have used this latter space group for DFT-D geometrical optimizations, at a theoretical temperature of 0 K, of model periodic structures for TPEA-F-HT with four different directions for the ethyl arms (**SI9**). We observe that these different orientations of the OSDA lead to silica frameworks with slightly different atom positions, highlighting the effect of OSDA-framework interactions. We can also retrieve an energy of stabilization for each of these models. The calculated energies point to a higher stabilization of the as-synthesized silicalite-1 when the ethyl arms are positioned in one single direction of the straight channel. However, the other possible locations for ethyl arms lead to stabilization energies that are only 20 to 30 kJ.mol<sup>-1</sup> higher (**SI9**). Therefore,

considering that the syntheses are partly governed by thermodynamics will lead to a preferential, but not exclusive, location of the ethyl arms in the straight channels with a specific location in these channels. And this could explain the experimental observations made above (XRD,  $^{13}\text{C}$  NMR).

We have thus shown consistently by different methods that ethyl arms of TPEA are preferentially located along [010] inside the straight pore channel of the MFI structure. However, two possibilities remain for the location of ethyl arms depending on the direction they follow in the straight channels and this could lead to different ordered or non-ordered arrangements. Ethyl arms could be located following a single direction in an ordered fashion (like in straight 1 and 2 model structures of **SI9**). But in this case the mirror symmetry of the space group *Pnma* is not effective, and another crystalline structure has to be determined by XRD. Furthermore, the crystal structure obtained at 100 K and the  $^{13}\text{C}$  NMR spectra are also more consistent with the presence of different locations for ethyl arms, the two directions along [010] being preferred. Another possible ordered arrangement could consist in ethyl arms following strictly alternating directions along [010]. The driving forces leading to this simultaneous arrangement of two OSDA molecules during the synthesis are difficult to envision, and this ordered arrangement corresponds again to another crystal structure, not found experimentally here. Therefore the non-ordered arrangement of ethyl arms along [010] is here the most probable.

#### ***Nature of the local geometrical disorder in the zeolite framework***

The similarities in the broadening of the  $^{29}\text{Si}$  NMR peaks observed for two silicalite-1 zeolites, TPA-F-SF and TPEA-F-HT (**Fig. 1C** and **1D**), prepared through slightly different routes could lead to a straightforward conclusion: both zeolites present the same kind of local geometrical disorder. There are however differences between them that bear information on the nature of local order or disorder. In particular, we observed that the two zeolites obtained in fluoride medium with TPA as OSDA undergo the m-o transition when decreasing *T*, but not the zeolite obtained with TPEA. In this latter case, the presence of local geometrical disorder could be invoked to explain a blocking of the transition, but this leaves unexplained why an apparent similar disorder does not have the same effect on TPA-F-SF.

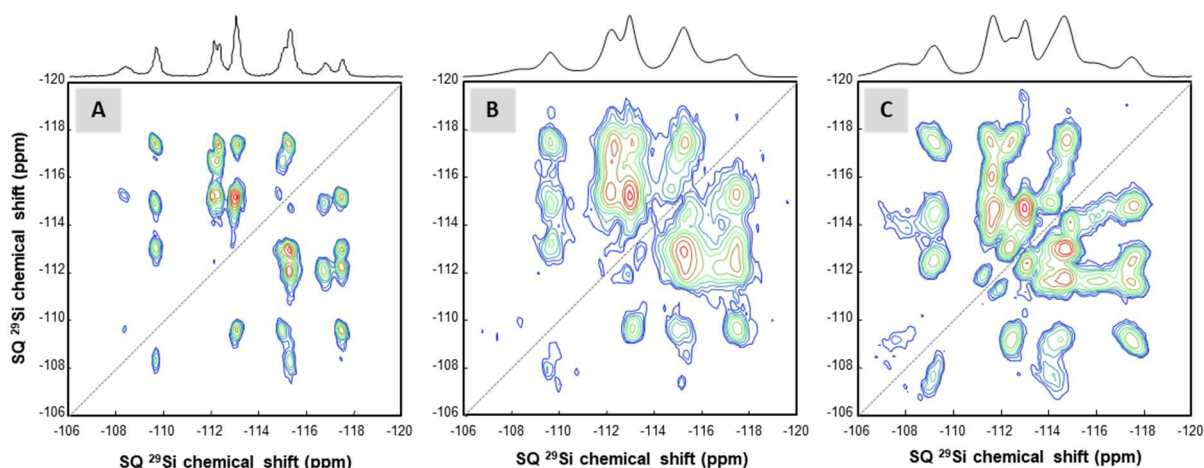


**Fig. 10.** 2D SQ-SQ  $^{29}\text{Si}$ - $^{29}\text{Si}\{^1\text{H}\}$  CP-INADEQUATE-MAS spectra of as-synthesized zeolites: (A) TPA-F-HT, (B) TPA-F-SF, (C) TPEA-F-HT. The 2D dataset are obtained after a shearing transformation of the recorded DQ-SQ correlations. Only the spectral region containing cross-peaks is presented (the  $^{29}\text{Si}$  exchange peak at ca -125 ppm, corresponding to T6 sites in interaction with F, does not yield any visible cross-peak). The contour lines of the three 2D spectra have been obtained with identical graphical parameters.

A detailed analysis of the 2D  $^{29}\text{Si}$ - $^{29}\text{Si}\{^1\text{H}\}$  CP-INADEQUATE spectra can give additional insights. The spectra of the zeolites obtained with a fluoride route are presented as single quantum-single quantum SQ-SQ correlations in **Fig. 10** (see **SI10** for details). In the case of more ordered TPA-F-HT, the cross-peaks are well defined and are almost separated one from another (**Fig. 10A**). This allowed the connectivity scheme of the Si units to be described and an assignment of the peaks to be proposed.<sup>46</sup> We remade this assignment (**Fig. 1B**, **SI11**) considering the INADEQUATE data, the study of Si-F distances<sup>46</sup> and the site numbering proposed by Chao *et al.*<sup>57</sup> In addition, it is of importance to remark that the rounded shapes of the cross-peaks testify of a small distribution of individual chemical shifts and thus of the geometrical order. These line-shapes are in contrast with what we observe for the two other zeolites TPA-F-SF and TPEA-F-HT where cross-peaks show elongated and ellipsoidal shapes with different slopes. As previously exemplified by Cadars *et al.*<sup>81</sup> such line-shapes reflect the probability of pairs of chemical shifts. A purely statistical random disorder would give vertical or horizontal elongations. When tilting of the ellipsoids' principal axes is observed, they are characteristic of underlying order in the local disorder or, in other words, preferential links in the pair distribution of sites. This is what we observe in the case of TPEA-F-HT (**Fig. 10C and 11**). We can thus evidence the presence of correlated geometrical disorder between neighboring Si units connected through a siloxane bond within the silica framework. This type of disorder implies that the two bound Si units cannot take independent geometrical configurations. Moreover, it is remarkable to notice that the cross-peaks of TPEA-F-HT are shifted with respect to the cross-peak positions for TPA-F-HT, while they are unchanged for TPA-F-SF (**Fig. 10B**, **SI10**). The slightly smaller size of the TPEA leads to a small contraction of the unit cell (**Fig. 2C**) and therefore to local modifications in Si-O and Si-O-Si bond distances and angles. In turn, these local modifications will affect the  $^{29}\text{Si}$  chemical shifts.<sup>82</sup> It is

noteworthy that this contraction does not operate uniformly as seen from the differences in cell parameters (**Fig. 2B**) and from the variations in  $^{29}\text{Si}$  chemical shifts' position and distribution. There are thus distinct effects of the smaller OSDA on the zeolite structure.

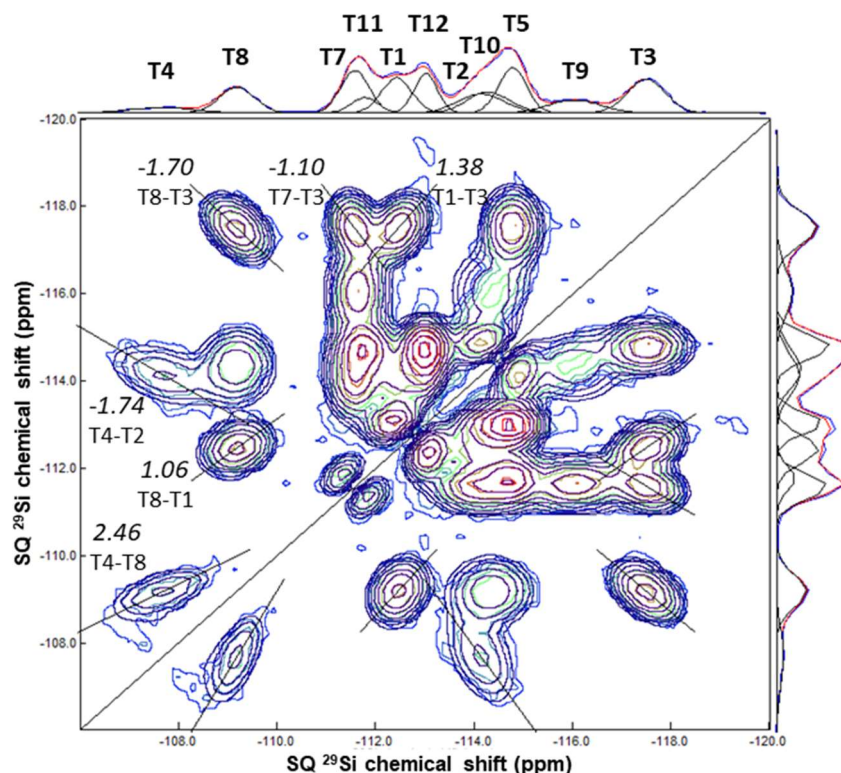


**Fig. 11.** 2D SQ-SQ  $^{29}\text{Si}$ - $^{29}\text{Si}\{^1\text{H}\}$  fitted CP-INADEQUATE-MAS spectra of TPEA-F-HT. The experimental SQ-SQ spectrum (multicolor contour plot) is symmetrized before fitting. Only the spectral region containing cross-peaks is presented (the  $^{29}\text{Si}$  exchange peak at ca -125 ppm, corresponding to T6 sites in interaction with F, does not yield any visible cross-peak). The model spectrum obtained by fit is presented as purple contour plot. The cross-peaks for which a correlated disorder can be modeled are marked with oblique lines and values of the order parameter (see text).

For a more detailed analysis, we fitted the  $^{29}\text{Si}$ - $^{29}\text{Si}$  INADEQUATE correlation spectra of TPA-F-HT and TPEA-F-HT. To this end, we used a home-developed method that accounts for the observed correlated disorder (**Fig. 11**). Both fits confirm (TPA) or lead to (TPEA) a full assignment of the  $^{29}\text{Si}$  resonances. It is possible to model the observed tilted cross-peaks taking the simplest hypothesis of a linear correlation between the distributions of chemical shifts of the connected sites. This introduces an *order parameter* whose sign correspond to the slope and whose magnitude to the degree of ordering from 0 for a statistical random disorder (horizontal or vertical ellipsoid) to infinity for an idealized perfectly ordered structure (infinitely sharp ridge). The values obtained from the fit are also presented in **Fig. 11**. The Si sites exhibiting a correlated disorder with neighboring sites (namely T1, T2, T3, T4, T7 and T8) are presented in **Fig. 12**. These sites are in close proximity to each other, forming

interconnected 5 MR and 6 MR cycles and chains that arrange into a column along the [010] direction (**Fig. 12B**).

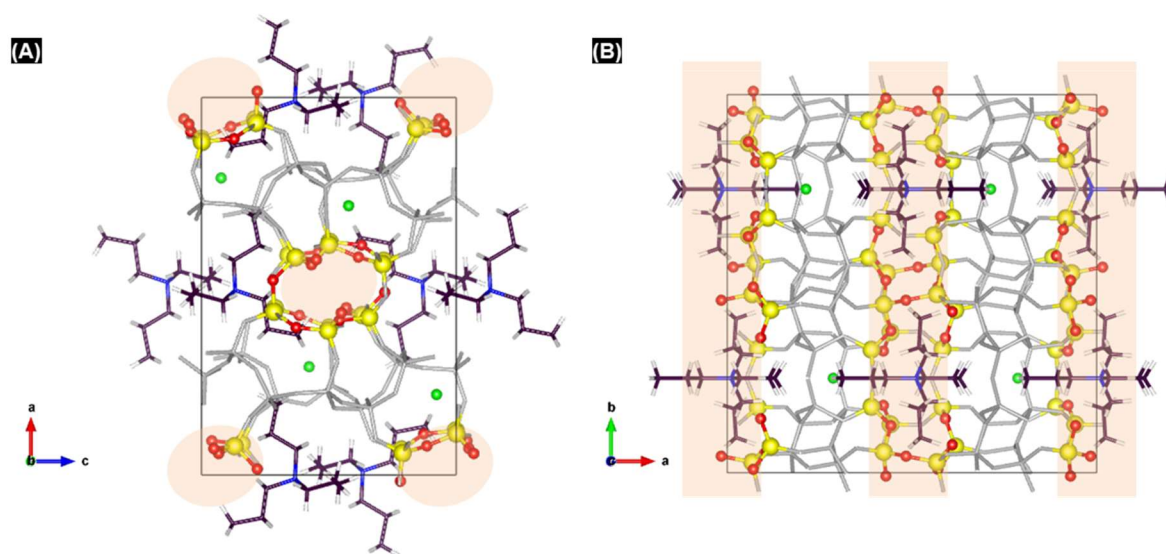


**Fig. 12.** Locations of Si sites (and related O Sites) presenting a correlated disorder with at least one of the neighboring Si sites: (A) projection on the *ac* plane, (B) projection on the *ab* plane. The locations are highlighted by the ball representation in the orange areas. Other atoms and bonds are represented by sticks. The colors follow mostly CPK convention (black, white, blue, red, yellow and green for C, H, N, O, Si and F respectively). The structure, used here for visualization, corresponds to a theoretical model for TPA-F silicalite-1 obtained by DFT geometry optimization (*Pnma* space group).

Additional information on the silica framework differences between TPA-F-HT and TPEA-F-HT above transition's temperatures can be gained from XRD. The cell parameters, along with the coordinates and anisotropic atomic displacement parameters (ADP) of Si, O and F atoms were obtained from refined structures for the framework of as-prepared silicalite-1 single crystals at 295 K. Owing to the difficulties encountered in determining the position of the OSDA molecules in these RT structures (opposed to structures analyzed at 100 K, *vide supra*), the space group considered here is *Pnma* that also provides more consistent refinements than *Pn2<sub>1</sub>a*. Very small differences are also noticed here between the cell parameters of these two zeolites (-0.1% in volume for TPEA-F-HT). More information is obtained from the displacement tensors [ $U_{ij}$ ]. In the case of TPA-F-HT, when looking at Si atoms, the highest  $U_{iso}$  values are found for Si that are the closest to F and forming the  $[4^15^26^2]$  cage (**SI12**). For the Si and O atoms close to F, the ellipsoids are pointing to the F positions. These results can be understood by the chemical exchange of F atoms between two positions, forming the  $[\text{SiO}_4\text{F}]$  units. This chemical exchange leads thus to geometrical modifications of the symmetry related atoms in the  $[4^15^26^2]$  cage, and to an enhanced thermal disorder at the vicinity of F. Consistently, we notice that Si atoms close to F in the  $[4^15^26^2]$  cage are also giving rise to the broadest  $^{29}\text{Si}$  NMR peaks (**Fig. SI13**). For TPEA-F-HT crystals of same quality, we systematically observe larger  $U_{iso}$  values for the Si and O atoms

(+4 to +25%) than for TPA-F-HT, while  $U_{iso}$  decreases for F (-38%). The silica framework presents thus a higher degree of geometrical disorder in case of TPEA-F-HT, but the differences in  $U_{iso}$  values between the two samples do not provide a rational trend.

Furthermore, anisotropic atomic displacement parameters (ADP) of TPA-F-HT and TPEA-F-HT can be compared following various approaches.<sup>83,84</sup> The analysis of the figure of merit (FOM) gives interesting insights. The FOM compares the ADPs of atoms measured at different temperatures, pressures, etc., or between equivalent atoms in isostructural compounds with respect to their orientation in space and size. The lower the FOM the more equivalent the ADPs are. When comparing the Si sites in TPA-F-HT and TPEA-F-HT structures (295 K), the highest FOM percentages, above 0.10 the mean value for Si (**Table SI14**), are obtained for four Si sites (T2, T3, T7 and T8). These are the sites that give the lowest fits between TPA-F-HT and TPEA-F-HT structures, and thus the most deformed sites when comparing these structures. Interestingly these most deformed sites also present a correlated disorder with neighboring sites in the  $^{29}\text{Si}$ - $^{29}\text{Si}$  INADEQUATE correlation spectra (*vide supra* and **Fig. 11**).

#### ***Guest effect on the degree of order of the silica host at RT***

When the zeolites are prepared with TPA and fluoride anions, the  $^{29}\text{Si}$  isotropic chemical shifts exhibit the same mean values for HT and SF synthesis methods. For the latter method  $^{29}\text{Si}$  NMR show wider distributions of chemical shifts and shorter transverse relaxation times  $T_2'$  (**SI2**). Both differences are understood as characteristic of a lower quality of the TPA-F-SF crystals compared to TPA-F-HT, and probably explained by a global disorder with the presence of more crystal defects and a wider distribution in geometrical parameters. The situation is different when a small chemical modification of the OSDA is introduced. Replacing TPA by TPEA has a great effect on the local ordering of the silica framework. However, the two zeolites TPA-F-HT and TPEA-F-HT share several common characteristics usually ascribed to a significant degree of order. The proportions of chemical defects like silanols are very small ( $^{29}\text{Si}$  NMR). Both zeolites have also a high degree of crystallinity (XRD, **SI3**), and thus long-range ordering, although the presence of the smaller TPEA leads to a smaller unit cell, demonstrating indirectly the presence of OSDA-framework interactions acting on the geometrical parameters. In addition,  $^{29}\text{Si}$  transverse relaxation times  $T_2'$  present similar long values (**Table SI2**), and both OSDAs present well defined NMR signatures ( $^{13}\text{C}$ ,  $^{14}\text{N}$ ) with similar motional processes in the 180-295 K temperature range. Finally, after removal of the OSDAs by calcination in air, the final zeolites present very similar structural characteristics (XRD,  $^{29}\text{Si}$  NMR). Therefore, the differences observed between these as-synthesized OSDA-zeolite assemblies have to be explained by subtle differences in the relative positioning and interactions between these OSDAs and the silica framework.

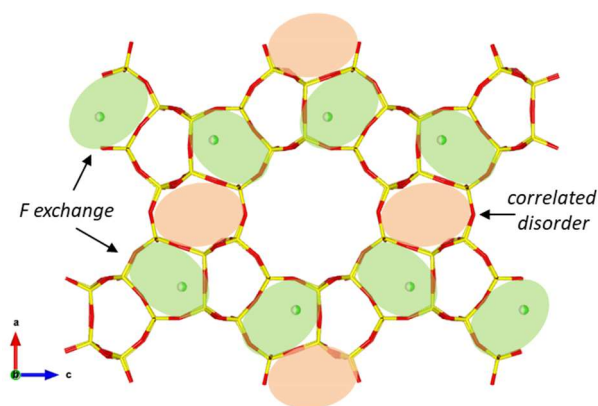


**Fig. 13.** Schematic representation of the two possible types of disorder identified in the silicalite-1 MFI framework for the orthorhombic phases (projection onto the *ac* plane): dynamical and geometrical disorder due to F site exchanges (green areas) and correlated geometrical disorder (orange areas). Atoms and bonds of the framework are presented by sticks (O in red, Si in yellow)

Two specific types of short-range disorder in these host-guest zeolites are found for the silica FWs and highlighted in **Fig. 13**. A first type involves the Si atoms located in the  $[4^15^26^2]$  cage containing F, and presenting a higher  $U_{iso}$  from the crystal structures and larger FWHM for their  $^{29}\text{Si}$  NMR peaks. It is related to the exchange of F atoms between Si sites, and its impact on the geometrical parameters (SiO bond distances and SiOSi angles). This type of dynamical and geometrical disorder is present in both types of zeolites. A second type of specific disorder is only observed for TPEA-F-HT. As evidenced by  $^{29}\text{Si}$  NMR INADEQUATE experiments, some distributions in  $\delta(^{29}\text{Si})$  are strongly correlated to the distributions of adjacent Si sites. In this case, the variations in the geometrical parameters of one site depend on that of the adjacent site. Herein, the geometrical variations of two correlated Si sites are not independent. In the unit cell, the Si sites subjected to this correlated disorder are forming columns along *b* (**Fig. 12** and **Fig. 13**). Most of them lead also to the worst FOM when comparing the ADP of Si sites in TPA-F-HT and TPEA-F-HT (XRD), and thus to the highest structural deviations between structures.

This second type of disorder can be related to the positioning of TPEA inside the zeolite. As mentioned, the nature and structure of the organic molecules hosted in silicalite-1 influences the geometry of the silica framework around them thanks to the interplay of various effective intermolecular interactions (van der Waals, Coulomb, hydrogen bonds).<sup>85-88</sup> These molecular effects are observed at a long-range length scale, typically by XRD, but their local nature obviously operates at the short range. Hence, each specific positioning of an ethyl arm will lead to a specific and local geometrical deformation of the silica framework. Meanwhile, this local deformation depends on energy minimization constraints operating at the different scale ranges: host-guest interactions at the level of the local OSDA-zeolite arrangement, and long-range host structure stabilization.

This interdependency between the local deformations and the surrounding silica framework might explain the nature of the correlated disorder created by TPEA. Because the ethyl arms are preferentially located along the  $[010]$  direction, the local deformations will mostly impact the siloxane

bonds forming chains along this direction. Depending on the internal stresses induced by these deformations, these bonds will show different degrees of correlated disorder. Within the orthorhombic *Pnma* silicalite-1 structure, there are two short chains C1 and C2 that cross the unit cell along *b* (red and blue atom sites in **Fig. 14A**). These chains link the Si sites T3-T4-T7-T8 (C1) and T5-T6-T11-T12 (C2). They present very similar geometries (distances, angles) and share common symmetry elements like the mirror normal to *b* axis. Their main difference lies in their relative positions within the structure. For C1, one chain is only bound to another of these chains, but of opposite direction, through T1 and T2 sites (represented in pink in **Fig. 14B**). These pair of C1 chains form exactly the columnar arrangement described above for the correlated disorder (**Fig. 12 and Fig. 13**). For C2, one chain is bound to two other chains of opposite direction (through T9 and T10 sites, pale blue in **Fig. 14B**), forming rather a layer parallel to the *bc* plane. This positioning in planes for C2 chains allows an easier adaptation to local deformations and a more efficient relaxation of the related stresses, than the columnar arrangement of C1 chains of opposite directions. For this latter case, the resulting higher stress induced by the deformations imposes the correlated disorder between Si sites observed by  $^{29}\text{Si}$  NMR, while none is observed for Si sites in the C2 chains forming planes.

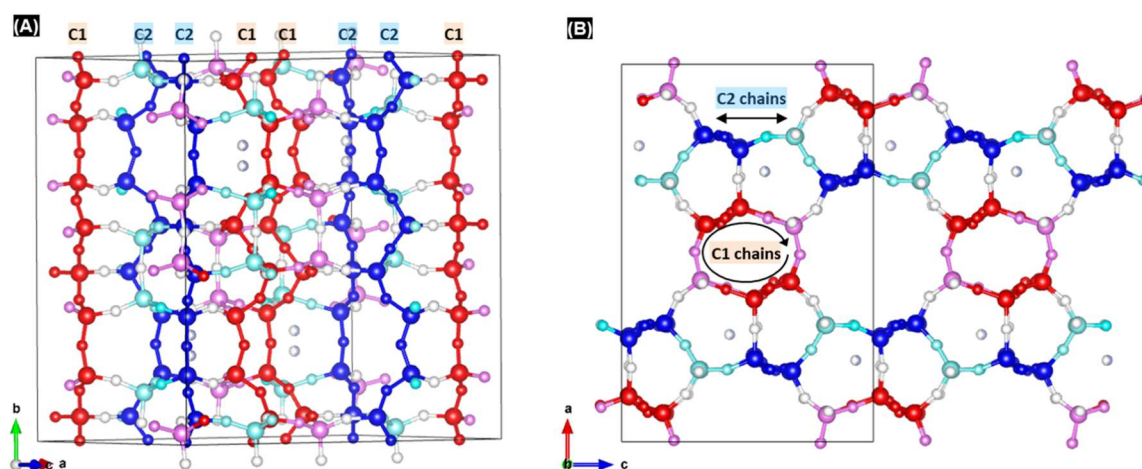


**Fig. 14.** Visualization of the siloxane chains crossing the crystal unit cell (black lines) along the [010] direction: (A) oblique view, (B) projection onto the *ac* plane. Si and O atoms are represented as balls colored in red (C1 chains), pink (connections between C1), blue (C2 chains) and pale blue (connections between C2). The arrows illustrate the two different connection between the chains. The structure, used here corresponds to the resolved structure of TPEA-F-HT at 295 K omitting the TPEA molecules.

### ***Guest effect of on the low *T* phase transition of the host***

The phase transformation between orthorhombic and monoclinic MFI phases is reversible and displacive without modifying the MFI topology,<sup>39</sup> and it has been simply modelled using free energy minimization schemes and interatomic potentials.<sup>89,90</sup> Thermodynamic studies of the m-o transitions in

porous ZSM-5 samples showed that this transition occur over a large temperature range involving rather small enthalpy changes ( $\Delta H$  between 2 and 20 kJ.mol<sup>-1</sup>) that depend on Al content.<sup>31,32,91</sup> The structures of monoclinic and orthorhombic porous silicalite-1 have been compared. The transition from o to m can be described by shifts of (010) layers along the c axis leading to geometrical variations within the zeolite framework. Among other symmetry elements, the mirror normal to b is absent and the [4<sup>1</sup>5<sup>2</sup>6<sup>2</sup>] cage is deformed. The shift of (010) pentasil layers was first explained by a distortion or rotation of the 4 MR and 6 MR interconnecting the layers.<sup>92</sup> Further, it has been shown that the largest modifications in SiOSi angles occur for the sites at the cross-section between the (100) and (010) pentasil layers.<sup>93</sup> The m-o transition of as-synthesized silicalite-1 (similar to our TPA-F-HT zeolite) has been described as being of the same nature as its porous counterparts.<sup>43</sup>

We observed a m-o phase transition by XRD for TPA-F-HT and TPA-F-SF, but not for TPA-OH-HT and TPEA-F-HT. The inhibition of the m-o transition for TPA-OH-HT can be easily explained by a high degree of local disorder promoted by a high density of chemical defects, following ideas developed by Marra *et al.*<sup>94</sup> However, the inhibition of the transition in the case of TPEA-F-HT is a more intriguing process because of its high similarity with TPA-F-HT in terms of crystallinity and chemical defects. The F site exchange has similar dynamics and leads to the same observations for both TPA-F-HT and TPEA-F-HT zeolites. This F site exchange has an activation energy ( $E_A \approx 4$  kJ.mol<sup>-1</sup>, see **SI4**) of the same order of magnitude than the enthalpy changes measured for the m-o transition in calcined porous samples. In addition, the slowdown of the site exchange will undoubtedly favor the transition by decreasing the dynamical disorder observed for both zeolites, and by promoting a breakdown of the mirror symmetry. However, the absence of transition for TPEA-F-HT demonstrates that other conditions are necessary for the m-o transition to occur in these host-guest OSDA-zeolites. Besides, we have also seen that the simple presence of disorder probed for instance by the broadening of <sup>29</sup>Si NMR peaks like in TPA-F-SF is not a sufficient condition to block the transition, although it can modify its characteristics (*vide supra*). Below the temperature where the m-o transition occurs ( $\approx 170$  K), we observe contrasted behaviors for TPA-F-HT and TPEA-F-HT. The four propyl arms of TPA have different conformations inside the monoclinic phase (<sup>13</sup>C NMR, XRD), and the whole TPA is less mobile than in the orthorhombic phase as shown in previous works, and here by <sup>13</sup>C and <sup>14</sup>N NMR. On the contrary, the absence of evolution of the NMR signatures of TPEA suggests that the intermediate state around the transition temperature is frozen. The same conclusion is drawn for the silica FW by the variations in <sup>29</sup>Si resonances (widths and chemical shifts), and Raman bands showing notably the splitting of the bands related to 5 MR, 6 MR and 10 MR if the transition occurs.

What does inhibit the transition for TPEA-F-HT is probably the presence of correlated geometrical disorder between Si sites created by the positioning of TPEA. To demonstrate that, we can first hypothesize that the known flexibility of the silicalite-1 FW will be highly decreased by the presence of Si sites that cannot be displaced independently from one another. In addition, these sites are all close one to each other and forming the above described columnar arrangement of C1 chains along

b (**Fig. 12 and 15**). This arrangement will increase the rigidity in this direction, that is theoretically smaller than that along the two other crystal directions.<sup>95</sup> If the proportion of highly strained regions is important, the displacements along b will be limited. Therefore the low  $T$  transition - based on a shift of (010) pentasil layers along c following one of the two possible directions  $b_1$  and  $b_2$  (**Fig. 15**) – will be hampered. The correlated disorder prevents then the cooperative displacement corresponding to the monoclinic spontaneous strain, characteristic of the ferroelastic orthorhombic-monoclinic phase transition.<sup>31</sup>

Additional insights are obtained by comparing the crystal structures determined at 295 and 100 K. Large variations in SiOSi angles are noticed for both TPA-F-HT and TPEA-F-HT zeolites, the mean values showing a similar angle decrease with cooling, in agreement with a small contraction of the crystallographic unit cells (**SI15**). As a general trend, the highest angle variations are related to the highest SiOSi angles ( $>170^\circ$ ) in the orthorhombic phase, as also shown previously for the m-o transition in porous silicalite-1.<sup>93</sup> However, this general similarity in SiOSi bond angle variations between zeolites is not enough for the transition to occur in the case of TPEA-F-HT. The explanation must be found by inspecting the bond angles between sites presenting a correlated geometrical disorder that would be those more concerned by mechanical stresses. For instance, we consider here the angle between T3 and T8 sites (**Fig. 15**) that corresponds to one of the most correlated pairs of Si atoms from the  $^{29}\text{Si}$  NMR analysis of TPEA-F-HT (**Fig. 11**). In the case of TPA-F-HT, this angle is  $168.2^\circ$  at 295 K ( $Pnma$ ) and it is split into smaller and higher values separated by  $2.9^\circ$  ( $165.9^\circ$ ,  $168.8^\circ$ ) at 100 K ( $P2_1n$ ). Such angle splitting, large and in opposite directions, would be difficult to achieve when the geometry of T3 and T8 sites cannot vary independently as in TPEA-F-HT. These sites are also forming 5 MR (T1-T3-T8-T4-T2) inside which four siloxane bonds present a correlated disorder (**Fig. 15**). Therefore, the bond angle variations in different directions necessary to the m-o transition will be almost unreachable for this 5 MR. Accordingly, no angle splitting of T3-O-T8 is observed for TPEA-F-HT between 295 and 100 K (**SI15**), preserving the mirror symmetry of the initial orthorhombic phase with the most consistent  $Pnma$  space group.

All together, we can conclude that TPA-F-HT and TPEA-F-HT present the same global trends at low  $T$  in terms of dynamics and geometrical parameters but the correlated geometrical disorder existing in the latter zeolite, due to the disorder in the positioning of the ethyl arms, forbids some of the local atomic displacements necessary for the m-o transition to occur.

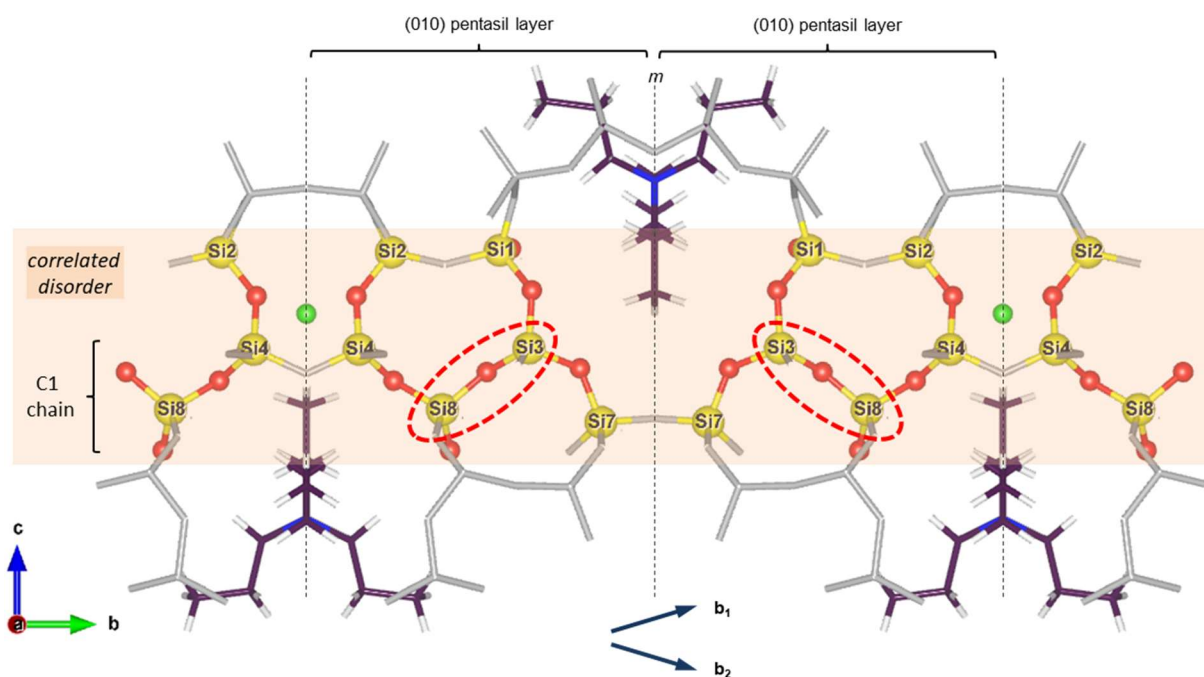


**Fig. 15.** Correlated disorder and orthorhombic-monoclinic transition. Si atoms presenting a correlated disorder, and the related O atoms, are represented as balls within the  $bc$  plane of the  $Pnma$  space group (DFT optimized model used here for visualization). The siloxane bonds between Si3 and Si8 (at the T3 and T8 sites), symmetric towards the  $m$  mirror, are highlighted by the red ellipses. Arrows  $b_1$  and  $b_2$  correspond to the possible directions of the  $b$  axis in the monoclinic phase. Other atoms and bonds are represented by sticks. The colors follow mostly CPK convention (black, white, blue, red, yellow and green for C, H, N, O, Si and F respectively). Si and O atoms not involved in the correlated disorder are greyed for the sake of clarity.

## MATERIALS AND METHODS

### *Syntheses*

*Precursors.* Tripropylethylammonium bromide (TPEABr) was synthesized using a Menschutkin reaction as previously described.<sup>54</sup> It was prepared by refluxing 0.1 mole of tripropylamine and 0.1 mole of ethylbromide in acetonitrile for 24 H. Then, the solution was cooled and the solvent was removed by rotary evaporation at reduced pressure. The recovered solid was re-crystallized in ethyl acetate, and washed with diethylether. Its purity was controlled by routine solution-state <sup>1</sup>H and <sup>13</sup>C NMR.

All the other reactants for zeolites' syntheses (fumed silica, silica gel, tetrapropylammonium bromide (TPABr), tetrapropylammonium hydroxide (TPAOH, 40 wt% water solution), and NH<sub>4</sub>F) were purchased from chemical companies (reagent grade) and employed without further purification.

*Zeolites.* The OSDA-silicalite-1 host-guest zeolites were obtained following and adapting known recipes. The solid raw precursors were dried before their use. After the thermal treatments, all the as-synthesized zeolites were recovered by filtration and dried over night at 353 K. TPA-OH-HT was obtained by mixing fumed silica, TPAOH and demineralized water with an initial gel composition of 1 SiO<sub>2</sub>:0.43 TPAOH:28 H<sub>2</sub>O. The resulting mixture was heated in a PTFE-lined autoclave at 448 K for 2 days. TPA-F-HT and TPEA-F-HT were obtained by mixing the OSDA precursor (TPABr or TPEABr) with fumed silica, NH<sub>4</sub>F and demineralized water with an initial gel composition of 1 SiO<sub>2</sub>:0.08 OSDA (TPABr or TPEABr):0.04 NH<sub>4</sub>F:20 H<sub>2</sub>O. The resulting mixture was heated in a PTFE-lined autoclave at 473 K. 15 days of hydrothermal treatment allowed to form very well defined single crystals completely filled by the OSDAs, for Raman spectroscopy and crystal structure determination,. A longer HT treatment for 30 days insured the formation of fully homogeneous polycrystalline samples with almost 100% incorporation of OSDA that were used for powder analyses. TPA-F-SF, the solvent-free zeolite, was synthesized adapting a previous protocol.<sup>96</sup> Silica gel, TPABr and NH<sub>4</sub>F were mixed and ground with a small amount of demineralized water (molar ratios of 1 SiO<sub>2</sub>:0.08 TPABr:0.15 NH<sub>4</sub>F:1.04 H<sub>2</sub>O) in an agate mortar for 15 minutes. The obtained powder was transferred to a Teflon-lined stainless-steel autoclave and heated at 448 K for ca. 5 days (111 H).

Preliminary analyses (TGA, EDX, XRD, NMR) confirm the formation of OSDA-silicalite-1 host-guest zeolites without impurities or secondary phases. The size of the crystalline silicalite-1 particles differ. While the more ordered TPA-F-HT zeolite crystals have a length of about 70-80 μm, using the solvent-free method yields 10-30 μm long crystals, replacing TPA by TPEA gives 50-60 μm long crystals and the TPA-OH-HT synthesis yielded small crystals with lengths about 0.3-0.4 μm.

After calcinations in air (thermal treatment for OSDA and F<sup>-</sup> removal), the differences in disorder observed by <sup>29</sup>Si NMR are attenuated. In particular, the calcined silicalite-1 obtained from TPEA-F-HT does not present broader <sup>29</sup>Si peaks than that obtained from TPA-F-HT.

### *X-ray diffraction*

#### *XRD - Powder*

X-ray powder diffraction measurements at low temperature were performed in an Oxford PheniX cryostat on a Malvern Panalytical Empyrean diffractometer with a PIXcell<sup>3D</sup> detector using Cu Kα (λ=1.5418 Å) and Co Kα radiation (λ=1.7903 Å). The MFI samples were ground using a McCrone X-ray mill and then placed in the sample

holder in the cryostat. Diffraction data were typically obtained over an angular range from 5° to 120° in 2 $\theta$ . The program Fullprof<sup>97,98</sup> was used to perform Le Bail fits in order to determine the unit cell parameters.

#### *XRD single crystal structure determinations*

All single crystal X-ray diffraction experiments were performed at the XRD2 structural biology beamline of Sincrotrone Elettra Trieste SCpA. The light source used by the beamline is a superconducting wiggler, and a wavelength  $\lambda = 0.7000 \text{ \AA}$  was selected using a cryogenically cooled dual crystal Si monochromator. The diffraction setup consisted of an Arinax MD2S high throughput diffractometer and a Pilatus 6M detector. The beam was defined using a 100  $\mu\text{m}$  aperture and further cleaned using a 200  $\mu\text{m}$  capillary, while the crystals were in an open flow nitrogen cryostat at 100K and 295 K. The diffraction data of three different crystals of both TPA-F-HT and TPEA-F-HT were collected, of which two at 100 K and 295 K and one at 100 K only.

For each of the samples a minimum of four crystals were tested in order to ensure data quality and to check the sample purity. A standard data collection was used, consisting of a 360°  $\phi$ -scan. Frame integration and scale and absorption corrections were done with *XDS* and space group assignment was provided by *Pointless* from the *CCP4* software suite,<sup>99</sup> as implemented in the *XDS4Elettra* interface. All collected datasets presented appreciable diffraction, i.e.  $\langle \sigma(I)/I \rangle > 2$  in the last 0.80-0.75  $\text{\AA}$  resolution shell.

All structural refinements were carried out with *SHELXL*<sup>80</sup> and proceeded as follows. For each of the datasets the cell parameters as found from the *XDS* data reduction software were replaced by those obtained from the powder diffraction experiments, since they were estimated to be of higher quality than those extracted from the integration of the single-crystal diffraction frames, which may be affected by twinning issues. Indeed, although the powder diffraction experiments clearly showed a monoclinic phase for TPA-F-HT at low temperatures, the single-crystal data reduction software was not capable to detect this, because of the occurrence of a pseudo-merohedral twin along the *b*-axis in the monoclinic spacegroup  $P2_1/n11$  (*a*-axis unique). The silicalite framework was anisotropically refined in the space groups *Pnma* and  $Pn2_1a$  for the data sets collected at 295 K and for the data sets of TPEA-F-HT at 100 K. For the data sets of TPA-F-HT at 100 K the refinements were performed using a model consisting of two independent pseudo-merohedral twins, with twin laws 010/-100/001 and -100/010/00-1, respectively. The reflection file for this case was prepared with the *2TWIN* script<sup>100</sup> and merged with the *MERGEHKL5* program.<sup>101</sup> In all cases the position of the fluorine counter ion was easily found from difference Fourier maps and its occupancy was freely refined. The refined occupancy gives an estimation about the quantity of positively charged OSDA inside the pores, since electroneutrality needs to be preserved, assuming that the silica framework is free from aluminium. Anisotropic displacement ellipsoids remained positive for all refinements. For the refinements in  $Pn2_1a$  the two independent fluorine positions were first removed from the structural model after which the difference Fourier map was inspected. In all cases two peaks of nearly equal height were found at the positions calculated from the model in *Pnma*. The refinement of the occupancies was, however, not stable. A constrained model of equal occupancies gave *R*-factors very close to those obtained in *Pnma*. Therefore the centrosymmetric model was preferred to the non-centrosymmetric model. The same approach for the fluorine anions was used for the refinement of TPA-F-HT at 100 K in space group  $P2_1/n11$ . This model appeared to be stable.

**Table 3.** Reports statistics of the data collections and reliability factors for the different refinements.

	$\langle I/\sigma(I) \rangle$	$R_{\text{int}}^a$	$R_{\text{redund}}^b$	Spgr <sup>c</sup>	$R_F$ ( $I/\sigma(I) > 2$ ) <sup>d</sup>	$R_F$ (all) <sup>d</sup>	$TF^e$	occ(F1) <sup>f</sup>	$\Delta\rho_{\text{max}}^g$
<b>TPA-F-HT</b>									
vv001_c1_1 (100 K)	17.09	0.069/0.066	0.074/0.079	$P2_1/n11$	0.0804	0.0809	0.494(4)/0.0042(11)/ 0.498(4)/0.0043(11)	0.319(7)	4.47
vv001_c1_4 (295 K)	23.04	0.054	0.057	$Pnma$	0.0612	0.0657	0.99676(12)	0.191(8)	2.19
vv001_c2_1 (100 K)	19.12	0.067/0.058	0.063/0.070	$P2_1/n11$	0.0861	0.1013	0.501(5)/0.0006(7)/ 0.498(5)/0.0002(7)	0.351(8)	4.47
vv001_c2_2 (295 K)	19.15	0.064	0.067	$Pnma$	0.0629	0.0676	0.99990(4)	0.165(7)	2.48
vv001_cr3 (100 K)	24.45	0.080/0.079	0.082/0.086	$P2_1/n11$	0.0873	0.0969	0.478(5)/0.0246(15)/ 0.476(4)/0.0216(15)	0.289(8)	3.73
<b>TPEA-F-HT</b>									
vv002_c1_1 (100 K)	15.83	0.087	0.092	$Pnma$	0.1187	0.1230	0.9699(8)	0.296(11)	3.789
vv002_c1_2 (295 K)	20.49	0.066	0.071	$Pnma$	0.1054	0.1099	0.99757(19)	0.207(10)	1.656
vv002_c2_1 (100 K)	21.78	0.062	0.066	$Pnma$	0.0758	0.0786	0.9926(3)	0.367(11)	4.699
vv002_c2_2 (295 K)	26.70	0.048	0.051	$Pnma$	0.0588	0.0621	0.99822(11)	0.208(8)	2.397
vv002_cr2 (100 K)	34.00	0.038	0.040	$Pnma$	0.0857	0.0914	0.9539(8)	0.386(13)	5.499

<sup>a</sup>  $R_{\text{int}} = \sum |I(\mathbf{h}, i) - I(\mathbf{h})| / \sum I(\mathbf{h}, i)$ . <sup>b</sup>  $R_{\text{redund}} = R_{\text{int}}$  corrected for redundancy;  $R_{\text{int}}$  and  $R_{\text{redund}}$  have been calculated using *XDS* and are with respect to space group  $Pnma$ ; for  $P2_1/n11$  they have been also calculated using *MERGEHKL5* with respect to monoclinic symmetry. The first value refers to orthorhombic symmetry and the second to monoclinic symmetry. <sup>c</sup> spgr is the space group symbol according to the Hermann–Mauguin notation. <sup>d</sup>  $R_F = \sum |F_{\text{obs}}(\mathbf{h}) - F_{\text{cal}}(\mathbf{h})| / \sum F_{\text{obs}}(\mathbf{h})$ . <sup>e</sup>  $TF$  is the major twin fraction when the space group is  $Pnma$ ; for space group  $P2_1/n11$  there are four twin fractions, the first value corresponds to twin law 100/010/001, the second to 010/-100/001, the third to -100/010/00-1 and the fourth to 010/100/00-1; note that twin fractions 0.494(4)/0.0042(11)/0.498(4)/0.0043(11) mean that the twinning with respect to  $a+b$  is almost absent, whereas that with respect to  $b$  gives almost equal twin domain volumes. <sup>f</sup> occ(F1) is the chemical occupancy of the fluorine site. In all cases the estimated standard deviation is reported within parentheses. <sup>g</sup>  $\Delta\rho_{\text{max}}$  is the maximum residual electron density in  $e/\text{\AA}^3$  found in the difference Fourier synthesis.

The twinning with respect to the two-fold rotation axis along  $a+b$  appears to be marginal in all cases, but the twinning of TPA-F-HT at 100 K with respect to the two-fold rotation axis around the  $b$ -axis in space group  $P2_1/n11$  is almost equipartitioned. Although the values of the occupancies of the fluorine sites are slightly correlated to the values of the atomic displacement parameters, the discrepancies between the results for the different crystals seem to be real, meaning that there is a certain variability in the filling of the pores by the OSDA. This is confirmed by the determination of the OSDA location in the different structures, which appears to be possible only for the crystals where the pores are best filled. We focus here therefore on the low-temperature

structures of vv001\_cr3 for TPA-F-HT and vv002\_cr2 for TPEA-F-HT (see **Table 3** for details). Further details of the crystal structure investigations may be obtained from the joint CCDC/FIZ Karlsruhe online deposition service: <https://www.ccdc.cam.ac.uk/structures/> by quoting the deposition numbers CSD-2110968-2110969. Supplementary data for the other partial refinements (Tables, Statistics ....) may be obtained upon reasonable request from the authors.

For the structure determination of TPA-F-HT at 100K, the twin model obtained during the refinement of the siloxane matrix was kept and refined during the successive cycles to determine the best location of the OSDA. The final OSDA model from the refinement of TPEA-F-HT in  $Pn2_1a$  was used as starting model, since TPA in  $P2_1/n11$  has also four independent arms. After some cycles it became clear that the C2 site was not split, and one split site was removed from the model. Since no clear signs of other split sites were found, the model was refined using one occupancy factor for the complete molecule, distance restraints between the covalently bonded atoms and atomic displacement similarity restraints (SIMU). During the last cycles hydrogen atoms were introduced at calculated positions. The final R-factors are  $R_F(I/\sigma(I)>2) = 0.0650$  and  $R_F = 0.0749$ , respectively. The final maximum and minimum electron density peaks in the difference Fourier map are 1.51 and -1.11 eÅ<sup>-3</sup>, respectively. The negative charge on the fluorine sites (0.74(1)) is nearly completely balanced by the positive charge on TPA (0.78(1)).

The Vesta software was used for the visualization and presentation of the crystal structures.<sup>102</sup>

### **Solid-state NMR**

**<sup>13</sup>C NMR.** Room temperature <sup>13</sup>C{<sup>1</sup>H} NMR CP-MAS spectra were recorded at  $\nu_0(^{13}\text{C}) \equiv 75.5$  and 150.8 MHz on Varian 300 and 600 spectrometers respectively, using 7.5 mm rotors spun at  $\nu_{MAS} = 5$  kHz. Variable temperature <sup>13</sup>C{<sup>1</sup>H} NMR CP-MAS spectra were recorded at  $\nu_0(^{13}\text{C}) \equiv 150.8$  MHz using 7.5 mm rotors spun at  $\nu_{MAS} = 3.5$  kHz. Experiments were conducted using a contact time  $\tau_c = 2.5$  ms, a linear ramp on the H contact pulse (~10 % slope), proton decoupling (continuous wave, CW) during acquisition, and a recycle delay of 4 s. The <sup>1</sup>H radio-frequency (RF) field strength  $\nu_{RF}$  was set to 42 kHz for CP and decoupling. Between 64 and 256 scans were acquired at each temperature.

**<sup>14</sup>N NMR.** Variable temperature <sup>14</sup>N NMR MAS single pulse spectra were recorded at  $\nu_0(^{14}\text{N}) \equiv 43.3$  MHz on a Varian 600 spectrometer using 7.5 mm rotors spun at  $\nu_{MAS} = 2.5$  kHz. <sup>14</sup>N  $\nu_{RF}$  was set to ~31 kHz, flip angles to  $\pi/8$  (2  $\mu$ s) and recycling delays to 0.1 s. These conditions ensure a wide irradiation, and proper longitudinal relaxation. The initial FID points were removed (left shift) such that Fourier Transform started at the top of the first rotational echo maximum. <sup>1</sup>H CW decoupling ( $\nu_{RF} \sim 25$  kHz) was used during <sup>14</sup>N acquisition. A room temperature <sup>14</sup>N NMR MAS single pulse spectrum was additionally recorded using a 9.5 mm rotor spun at  $\nu_{MAS} = 2.0$  kHz (other conditions remaining equal) for TPEA-F-HT in order to get a reference spectrum with a higher S/N.

**<sup>29</sup>Si NMR.** Room temperature <sup>29</sup>Si{<sup>1</sup>H} NMR CP-MAS and <sup>29</sup>Si-<sup>29</sup>Si{<sup>1</sup>H} 2D CP-INADEQUATE spectra were recorded at  $\nu_0(^{29}\text{Si}) \equiv 79.5$  MHz on a Varian 400 spectrometer using 7.5 mm rotors spun at  $\nu_{MAS} = 5$  kHz. For the CP-INADEQUATE experiments,<sup>103</sup> the delays for the excitation of the DQ transitions were optimized and comprised between 18 and 20 ms. <sup>1</sup>H decoupling was applied during the INADEQUATE block (CW,  $\nu_{RF} \approx 25$  kHz) and acquisition (Spinal-64,  $\nu_{RF} \approx 22$  kHz). For the CP block, a contact time  $\tau_c = 20$  ms and a linear ramp on the H contact pulse (~10% slope,  $\nu_{RF} \approx 50$  kHz) were used. Between 60 and 120 complex F1 datapoints were recorded. The number of scans was between 272 and 400, and the recycle delays fixed at 5 s. Variable temperature

$^{29}\text{Si}\{^1\text{H}\}$  NMR CP-MAS spectra were recorded at  $\nu_0(^{29}\text{Si}) \equiv 119.2$  MHz on a Varian 600 spectrometer using 7.5 mm rotors spun at  $\nu_{MAS}$  between 2.5 and 3.5 kHz. Experiments were conducted using a contact time  $\tau_c = 5$  ms, a linear ramp on the H contact pulse ( $\sim 10\%$  slope), proton decoupling (CW) during acquisition, and a recycle delay of 5 s.  $^1\text{H}$   $\nu_{RF}$  was set to 42 kHz for CP and decoupling. Between 16 and 128 scans were acquired at each temperature. Besides,  $T_2'$  ( $^{29}\text{Si}$ ) were measured using a CP-MAS block chained by a spin echo with  $^1\text{H}$  decoupling. Chemical shifts were referenced towards external neat TMS ( $^{13}\text{C}$ ,  $^{29}\text{Si}$ ) and solid  $\text{NH}_4\text{Cl}$  spun at 3 kHz ( $^{14}\text{N}$ ).

*Variable Temperature experiments.*  $\text{N}_2$  gas was used for VT MAS experiments. In a typical experiment, the sample is cooled down to 133 K, equilibrated and then analyzed at the different temperatures. MAS frequencies  $\nu_{MAS}$  were kept to small values in order to avoid an excessive consumption of liquid nitrogen used to cool down  $\text{N}_2$  gas. When needed, two spectra at different  $\nu_{MAS}$  were recorded to differentiate the isotrope peaks and the SSBs.  $\text{Pb}(\text{NO}_3)_2$  was used for the temperature calibration following a previously published procedure.<sup>104</sup>

*NMR spectrum fitting.* NMR spectra were analyzed and fitted using the freely available *DmFit* software.<sup>105,106</sup>  $^{14}\text{N}$  NMR spectra were fitted using a set of quadrupolar parameters ( $C_Q$ ,  $\eta_Q$ ) with the quadrupolar interaction being described at the first order (sufficient for the systems under study). The quadrupolar coupling constant  $C_Q$  and the asymmetry parameter  $\eta_Q$  are defined as follows by the principal values  $V_{ii}$  of the electric field gradient tensor:  $C_Q = eQV_{33}/h$  and  $\eta_Q = (V_{22} - V_{11})/V_{33}$  where  $h$  is Planck's constant and  $Q$ , the nuclear quadrupolar moment, and with  $|V_{33}| > |V_{11}| > |V_{22}|$ . The mathematical function used for fitting is implemented in the *DmFit* software and named *QUAD1st*.

$^{29}\text{Si}$ - $^{29}\text{Si}\{^1\text{H}\}$  2D CP-INADEQUATE spectra were fitted with a new approach. When considering ideally and perfectly ordered crystal structures, NMR 1D lines present Lorentzian profiles accounting for transverse relaxation phenomena. Their related cross-peaks in 2D correlation experiments appear as diamond 2D line shapes like in liquid-state NMR experiments. In the case of real solid materials the width of NMR 1D lines obtained under magic angle spinning (MAS) are most often dominated by a distribution of the isotropic chemical shift typically leading to gaussian profiles for a random distribution. The correlation cross-peaks then appear as vertical or horizontal ellipsoids whose principal axis correspond to the linewidth of the correlated peaks (Eq. 1).

$$S(x, y) = \text{Gauss}(x, w_x) \cdot \text{Gauss}(y, w_y) \text{ where Gauss stands for a gaussian function and } w \text{ for its width} \quad (1)$$

In their seminal work Cadars and co-authors interpreted the shapes of correlation cross-peaks in terms of conditional probability that departs from a purely statistical random distribution.<sup>81,107,108</sup> In the present work, we chose to model the observed cross-peaks by introducing the simplest possible hypothesis of a linear correlation between the distributions of chemical shifts of the two correlated peaks.

The function described below accounts for the correlation by introducing a single *correlation* or *order parameter*  $\alpha$ . This modeling is implemented in the *DmFit* program and available to users since version #20211104.

$$S(x, y) = \text{Gauss}(x, w_x) \cdot \text{Gauss}(y, w_y) \cdot \text{Corr}(\alpha, x, w_x, y, w_y) \quad (2)$$

with

$$\text{Corr}(\alpha, x, w_x, y, w_y) = \text{Gauss}(x \cdot (w_y / w_x)^{1/2} - \text{Sign}(\alpha) \cdot y \cdot (w_x / w_y)^{1/2}, (w_x + w_y) / \alpha) \quad (3)$$

The sign of the  $\alpha$  parameter [ $\text{Sign}(\alpha)$ ] will give the positive or negative bias of the cross-peak and the absolute value of  $\alpha$  will be 0 for a purely random correlation (equivalent to equation 1) and infinity for a perfect correlation (infinitely sharp ridge). The function is continuous from -infinity to +infinity and preserves the projections on both axis.

This 2D spectrum fitting approach of the correlated disorder, based on a linear correlation between the distributions in chemical shifts, involves a single additional parameter and is robust enough to reliably fit all the experimental recorded data (e.g. **Fig. 11**).

### ***Raman spectroscopy***

Raman experiments were performed with a Jobin-Yvon T64000 triple monochromator equipped with an Olympus microscope and a charge-coupled device cooled down to 140 K and a 532 nm diode laser. An Oxford Instrument Microstat closed-cycle helium cryostat was used for the low temperature measurements from 10–295K. The TPA-F-HT and TPEA-F-HT single crystals were fixed to the cold finger using silver paste. The temperature was measured near the sample using a silicon diode.

Based on group theory, the framework of orthorhombic MFI gives rise to 432 Raman-active modes of vibrations as follows: 110  $A_g$  + 106  $B_{1g}$  + 110  $B_{2g}$  and 106  $B_{3g}$ .<sup>65</sup> The OSDA will also contribute, TPA with  $S_4$  symmetry will give rise to 29 A + 30 B + 29 E modes.<sup>63</sup> This symmetry is broken in the case of TPEA leading to the absence of degenerate modes and will also have 9 fundamental modes less due to the replacement of a propyl by an ethyl group. Due to the configurational (dynamic and/or static) disorder present, certain site ( $C_s$ ) and factor group ( $D_{2h}$ ) splittings will not always be observed.

### ***DFT-D optimization of crystal structures***

The periodic density-functional theory (DFT) based calculations were carried out with *Crystal09* computer program. In all the calculations, empirical London dispersion (D) energy term  $E_d = -s_6 \sum_g \sum_{i,j} f_d^{ij}(R_{ij,g}) C_6^{ij} R_{ij,g}^{-6}$  was added following the scheme implemented in *Crystal09* code.<sup>109</sup> The cut-off value we used to truncate the summation over lattice vector,  $g$ , is 25.0 Å. The parameters in the empirical  $E_d$  formula are taken from ref.<sup>110</sup> and are the following:  $s_6 = 0.75$ ;  $f_d^{ij}(R_{ij}) = \left(1 + e^{-d(R_{ij}/R_i - 1)}\right)^{-1} = 20$ ; the atomic van der Waals radii  $R_i$  and atomic coefficients  $C_6^i$  are taken from Table 1 in the same reference.

The  $Pn2_1a$  space group, proposed early for an Al-ZSM-5 zeolite,<sup>111</sup> allows to accommodate the symmetry of OSDAs (TPA, TPEA) and zeolite framework (see Results and Discussion section). It is used here to explore the different orientations of the ethyl arms. Full geometrical optimizations (atomic positions and unit-cell parameters) were carried out. Basis functions of double- $\zeta$  quality were used to describe all atoms as follows: 6-31d1 for O, N, C and H,<sup>112</sup> 7-311g for F,<sup>113</sup> and Pople's basis set with polarization for Si.<sup>114</sup> The generalized gradient-corrected PBE approximation was used for the exchange correlation functional.

## CONCLUSIONS

We have investigated the nanoscale disorder in host-guest OSDA-silicalite-1 zeolites thanks to an extensive short- and long-range characterization enabling a molecular level understanding. The replacement of tetrapropylammonium TPA by the slightly smaller tripropylethylammonium TPEA in the hydrothermal synthesis of silicalite-1 using a fluoride route leads to a disorder in the positioning of TPEA. In turn, this promotes a correlated geometrical disorder between Si of the zeolite framework and a concomitant inhibition of the low  $T$  phase transition.

From  $^{13}\text{C}$  NMR, XRD and DFT data, we have shown that the ethyl arms of TPEA are located in a disordered fashion along the two directions of the straight channels of the zeolite assembly (b axis). This location promotes deformations for the Si sites located in one type of siloxane chain running parallel to the b axis that cannot relax the related stress. The sites involved in these chains experience a correlated disorder determined by fitting and analyzing  $^{29}\text{Si}$ - $^{29}\text{Si}$  2D CP-INADEQUATE spectra. Most of these sites also show the highest structure deformations obtained by the analysis of ADP retrieved from XRD data.

When cooling down the TPEA-silicalite-1 host-guest assembly before the usual monoclinic-orthorhombic transition temperature ( $T > 180$  K), the same processes observed for its TPA counterpart are observed: reduced motions of the OSDA and freezing of the F exchange dynamics. At lower temperatures ( $T < 180$  K), the collective displacement accompanying the m-o transition is not possible for the TPEA zeolite. The hosted TPEA molecule remains in a frozen-like state (Raman,  $^{13}\text{C}$  and  $^{14}\text{N}$  NMR), and the usual geometrical distortion of the silicalite-1 is not observed (Raman,  $^{29}\text{Si}$  NMR). From an analysis of the structural modifications necessary to the m-o transition, we demonstrate how the correlated geometrical disorder is responsible for blocking this transformation, maintaining the host-guest assembly in a more symmetric crystal phase.

The correlated disorder promoted here using a slightly smaller and less symmetric OSDA is of different nature of that observed for other TPA-silicalite-1 host-guest assemblies. When a solvent-free synthesis method is used, crystals presenting a low statistical geometric disorder are obtained which still present a low  $T$  m-o transition although with slightly different cell parameters. When a hydroxide route is used, the inhibition of the low  $T$  transition is easily explained by the high level of chemical and geometrical defects deduced from the  $^{29}\text{Si}$  NMR spectrum.

To our knowledge, this is the first time that such a drastic effect of a small guest's modification on a zeolite phase transition is evidenced and explained by the presence of correlated geometrical disorder within the host framework. This novel result might be extended to other systems opening new perspectives in the design of materials with tuned properties through the control and exploitation of correlated disorder.<sup>115</sup>

## **ACKNOWLEDGEMENTS**

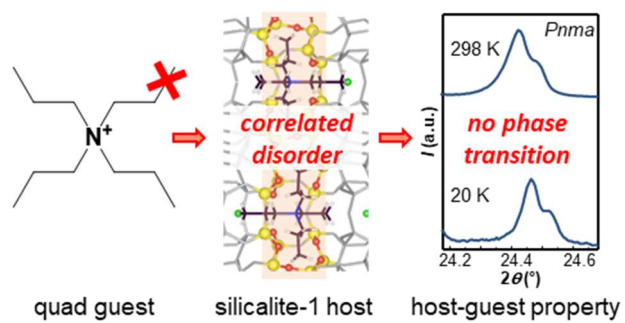
The French National Research Agency (ANR) is acknowledged for funding this research through the projects ZEOORG ANR-19-CE29-0008-01 and CheMISyst ANR-10-LABX-05-01. A.G. and T.M. acknowledge the granted access by GENCI to the HPC resources of CCRT/CINES/IDRIS (allocation A0070807369). S.A. thanks the Erasmus Mundus scholarship under the program: Erasmus Mundus Master in Membrane Engineering for a Sustainable World (EM3E-4SW), Project Number- 574441-EPP-1-2016-1-FR-EPPKA1-JMD-MOB. A.G. thanks the Erasmus Mundus Master in Materials Science Exploring Large Scale Facilities (MaMaSELF) program, PhilFrance Scholarships, and the University of the Philippines for scholarship and financial support. L.P. acknowledges financial support from the Swiss National Science Foundation (Early Postdoc Mobility scholarship, P2EYP2\_188002).

## **SUPPORTING INFORMATION CONTENT**

Numbering of Si sites; XRPD patterns of TPA-F-HT and TPEA-F-HT; complementary<sup>13</sup>C and <sup>29</sup>Si SSNMR data (spectrum comparisons, NMR parameters); DFT optimized structures and stabilization energies; anisotropy displacement parameters of TPA-F-HT and TPEA-F-HT structures; SiOSi angle variations between crystal structures.

This material is available free of charge via the Internet at <http://pubs.acs.org>.

## TABLE OF CONTENT



Host-Guest MFI Zeolites: Correlated Disorder and Phase Transition Inhibition by a Small Guest Modification

## REFERENCES

1. Breck, D. W., *Zeolite Molecular Sieves: Structure, Chemistry, and Use*. Wiley: New York, USA, 1973.
2. Barrer, R. M., *Zeolites and Clay Minerals as Sorbents and Molecular Sieves*. Academic Press: London, UK, 1978.
3. Davis, M. E., Ordered Porous Materials for Emerging Applications. *Nature* **2002**, 417, 813-821.
4. Yilmaz, B.; Müller, U., Catalytic Applications of Zeolites in Chemical Industry. *Top. Catal.* **2009**, 52, 888-895.
5. Martínez, C.; Corma, A., Inorganic Molecular Sieves: Preparation, Modification and Industrial Application in Catalytic Processes. *Coord. Chem. Rev.* **2011**, 255, 1558-1580.
6. Li, Y.; Li, L.; Yu, J., Applications of Zeolites in Sustainable Chemistry. *Chem* **2017**, 3, 928-949.
7. Bacakova, L.; Vandrovцова, M.; Kopova, I.; Jirka, I., Applications of Zeolites in Biotechnology and Medicine – a review. *Biomater. Sci.* **2018**, 6, 974-989.
8. Baerlocher, C.; Weber, T.; McCusker, L. B.; Palatinus, L.; Zones, S. I., Unraveling the Perplexing Structure of the Zeolite SSZ-57. *Science* **2011**, 333, 1134-1137.
9. Zones, S. I.; Chen, C. Y.; Benin, A.; Hwang, S.-J., Opportunities for Selective Catalysis within Discrete Portions of Zeolites: The case for SSZ-57LP. *J. Catal.* **2013**, 308, 213-225.
10. Jo, D.; Zhao, J.; Cho, J.; Lee, J.-H.; Liu, Y.; Liu, C.-H.; Zou, X.; Hong, S. B., PST-24: A Zeolite with Varying Intracrystalline Channel Dimensionality. *Angew. Chem. Int. Ed.* **2020**, 59, 17691-17696.
11. Roth, W. J.; Nachtigall, P.; Morris, R. E.; Čejka, J., Two-Dimensional Zeolites: Current Status and Perspectives. *Chem. Rev.* **2014**, 114, 4807-4837.
12. Wheatley, P. S.; Chlubná-Eliášová, P.; Greer, H.; Zhou, W.; Seymour, V. R.; Dawson, D. M.; Ashbrook, S. E.; Pinar, A. B.; McCusker, L. B.; Opanasenko, M.; Čejka, J.; Morris, R. E., Zeolites with Continuously Tuneable Porosity. *Angew. Chem. Int. Ed.* **2014**, 53, 13210-13214.
13. Hong, S. B.; Lee, S.-H.; Shin, C.-H.; Woo, A. J.; Alvarez, L. J.; Zicovich-Wilson, C. M.; Cambor, M. A., In Situ Disorder–Order Transformation in Synthetic Gallosilicate Zeolites with the NAT Topology. *J. Am. Chem. Soc.* **2004**, 126, 13742-13751.
14. Shin, J.; Bhange, D. S.; Cambor, M. A.; Lee, Y.; Kim, W. J.; Nam, I.-S.; Hong, S. B., Tetrahedral Atom Ordering in a Zeolite Framework: A Key Factor Affecting Its Physicochemical Properties. *J. Am. Chem. Soc.* **2011**, 133, 10587-10598.
15. Kim, H.; Cho, H. S.; Kim, C.; Choi, M., Gradual Disordering of LTA Zeolite for Continuous Tuning of the Molecular Sieving Effect. *J. Phys. Chem. C* **2017**, 121, 6807-6812.
16. Qin, Z.; Melinte, G.; Gilson, J.-P.; Jaber, M.; Bozhilov, K.; Boullay, P.; Mintova, S.; Ersen, O.; Valchev, V., The Mosaic Structure of Zeolite Crystals. *Angew. Chem. Int. Ed.* **2016**, 55, 15049-15052.
17. Qin, Z.; Hafiz, L.; Shen, Y.; VanDaele, S.; Boullay, P.; Ruaux, V.; Mintova, S.; Gilson, J.-P.; Valchev, V., Defect-Engineered Zeolite Porosity and Accessibility. *J. Mater. Chem. A* **2020**, 8, 3621-3631.
18. Li, T.; Ihli, J.; Wennmacher, J. T. C.; Krumeich, F.; vanBokhoven, J. A., The Link between ZSM-5 Zeolite Crystallization and Mesopore Formation by Leaching. *Chem. Eur. J.* **2019**, 25, 7689-7694.
19. Greaves, G. N.; Meneau, F.; Sapelkin, A.; Colyer, L. M.; ap Gwynn, I.; Wade, S.; Sankar, G., The Rheology of Collapsing Zeolites Amorphized by Temperature and Pressure. *Nat. Mater.* **2003**, 2, 622-629.

20. Haines, J.; Levelut, C.; Isambert, A.; Hébert, P.; Kohara, S.; Keen, D. A.; Hammouda, T.; Andrault, D., Topologically Ordered Amorphous Silica Obtained from the Collapsed Siliceous Zeolite, Silicalite-1-F: A Step toward “Perfect” Glasses. *J. Am. Chem. Soc.* **2009**, 131, 12333-12338.
21. Haines, J.; Cambon, O.; Levelut, C.; Santoro, M.; Gorelli, F.; Garbarino, G., Deactivation of Pressure-Induced Amorphization in Silicalite SiO<sub>2</sub> by Insertion of Guest Species. *J. Am. Chem. Soc.* **2010**, 132, 8860-8861.
22. Coasne, B.; Haines, J.; Levelut, C.; Cambon, O.; Santoro, M.; Gorelli, F.; Garbarino, G., Enhanced mechanical strength of zeolites by adsorption of guest molecules. *Phys. Chem. Chem. Phys.* **2011**, 13, 20096-20099.
23. Vezzalini, G.; Arletti, R.; Quartieri, S., High-Pressure-Induced Structural Changes, Amorphization and Molecule Penetration in MFI Microporous Materials: a Review. *Acta Cryst. B* **2014**, 70, 444-451.
24. Richard, J.; Cid, S. L.; Rouquette, J.; van der Lee, A.; Bernard, S.; Haines, J., Pressure-Induced Insertion of Ammonia Borane in the Siliceous Zeolite, Silicalite-1F. *J. Phys. Chem. C* **2016**, 120, 9334-9340.
25. Santoro, M.; Gorelli, F. A.; Bini, R.; Haines, J., Intermolecular Interactions in Highly Disordered, Confined Dense N<sub>2</sub>. *J. Phys. Chem. Lett.* **2017**, 8, 2406-2411.
26. Xu, W.; Liu, X. D.; Pena-Alvarez, M.; Jiang, H. C.; Dalladay-Simpson, P.; Coasne, B.; Haines, J.; Gregoryanz, E.; Santoro, M., High-Pressure Insertion of Dense H<sub>2</sub> into a Model Zeolite. *J. Phys. Chem. C* **2021**, 125, 7511-7517.
27. Fyfe, C. A.; O'Brien, J. H.; Strobl, H., Ultra-High Resolution <sup>29</sup>Si MAS NMR Spectra of Highly Siliceous Zeolites. *Nature* **1987**, 326, 281-283.
28. Hay, D. G.; Jaeger, H., Orthorhombic-Monoclinic Phase Changes in ZSM-5 Zeolite/Silicalite. *J. Chem. Soc. Chem. Commun.* **1984**, 1433.
29. Fyfe, C. A.; Kennedy, G. J.; Kokotailo, G. T.; Lyerla, J. R.; Fleming, W. W., The Effect of Temperature on the <sup>29</sup>Si Magic Angle Spinning N.M.R. Spectrum of Highly Siliceous ZSM-5. *J. Chem. Soc. Chem. Commun.* **1985**, 740-742.
30. Hay, D. G.; Jaeger, H.; West, G. W., Examination of the Monoclinic/Orthorhombic Transition in Silicalite Using XRD and Silicon NMR. *J. Phys. Chem.* **1985**, 89, 1070-1072.
31. Ardit, M.; Martucci, A.; Cruciani, G., Monoclinic–Orthorhombic Phase Transition in ZSM-5 Zeolite: Spontaneous Strain Variation and Thermodynamic Properties. *J. Phys. Chem. C* **2015**, 119, 7351-7359.
32. Mentzen, B. F.; Letoffe, J.-M.; Claudy, P., Enthalpy Change and Temperature of the Reversible Monoclinic-Orthorhombic Phase Transition in MFI type Zeolitic Materials. *Thermochim. Acta* **1996**, 288, 1-7.
33. Han, O. H.; Kim, C. S.; Hong, S. B., Direct Evidence for the Nonrandom Nature of Al Substitution in Zeolite ZSM-5: An Investigation by Al-27 MAS and MQ MAS NMR. *Angew. Chem. Int. Ed.* **2002**, 41, 469-472.
34. Sklenak, S.; Dedecek, J.; Li, C. B.; Wichterlova, B.; Gabova, V.; Sierka, M.; Sauer, J., Aluminum Siting in Silicon-Rich Zeolite Frameworks: A Combined High-Resolution Al-27 NMR Spectroscopy and Quantum Mechanics/Molecular Mechanics Study of ZSM-5. *Angew. Chem. Int. Ed.* **2007**, 46, 7286-7289.
35. Dib, E.; Mineva, T.; Véron, E.; Sarou-Kanian, V.; Fayon, F.; Alonso, B., ZSM-5 Zeolite: Complete Al Bond Connectivity and Implications on Structure Formation from Solid-State NMR and Quantum Chemistry Calculations. *J. Phys. Chem. Lett.* **2018**, 9, 19-24.

36. Fyfe, C. A.; Gobbi, G. C.; Murphy, W. J.; Ozubko, R. S.; Slack, D. A., Investigation of the Contributions to the Silicon-29 MAS NMR Line Widths of Zeolites and Detection of Crystallographically Inequivalent Sites by the Study of Highly Siliceous Zeolites. *J. Am. Chem. Soc.* **1984**, 106, 4435-4438.
37. Fyfe, C. A.; Strobl, H.; Kokotailo, G. T.; Kennedy, G. J.; Barlow, G. E., Ultra-High-Resolution Si-29 Solid-State Mas Nmr Investigation of Sorbate and Temperature-Induced Changes in the Lattice Structure of Zeolite Zsm-5. *J. Am. Chem. Soc.* **1988**, 110, 3373-3380.
38. Dib, E.; Mineva, T.; Gaveau, P.; Véron, E.; Sarou-Kanian, V.; Fayon, F.; Alonso, B., Probing Disorder in Al-ZSM-5 Zeolites by <sup>14</sup>N NMR Spectroscopy. *J. Phys. Chem. C* **2017**, 121, 15831-15841.
39. Wu, E. L.; Lawton, S. L.; Olson, D. H.; Rohrman Jr., A. C.; Kokotailo, G. T., ZSM-5-Type Materials. Factors Affecting Crystal Symmetry. *J. Phys. Chem.* **1979**, 83, 2777-2781.
40. Fyfe, C. A.; Kennedy, G. J.; DeSchutter, C. T.; Kokotailo, G. T., Sorbate-Induced Structural Changes in ZSM-5 (Silicalite). *J. Chem. Soc. Chem. Commun.* **1984**, 541-542.
41. Guth, J. L.; Kessler, H.; Wey, R., New Route to Pentasil-Type Zeolites Using a Non Alkaline Medium in the Presence of Fluoride Ions. *Stud. Surf. Sci. Catal.* **1986**, 28, 121-128.
42. Chezeau, J. M.; Delmotte, L.; Guth, J. L.; Soulard, M., High-Resolution Solid-State Si-29 and C-13 Nmr on Highly Siliceous Mfi-Type Zeolites Synthesized in Nonalkaline Fluoride Medium. *Zeolites* **1989**, 9, 78-80.
43. Chezeau, J. M.; Delmotte, L.; Hasebe, T.; Chanh, N. B., Low Temperature Orthorhombic-Monoclinic Transition in As-Synthesized MFI Siliceous Zeolites. *Zeolites* **1991**, 11, 729-731.
44. Mentzen, B. F.; Sacerdote-Peronnet, M.; Guth, J. L.; Kessler, H., Characterization of the Fluoride Anion by X-Ray-Powder Diffraction in an Mfi Tpf Zeolitic Material Prepared in Fluoride Medium. *C. R. Acad. Sci.* **1991**, 313, 177-182.
45. Koller, H.; Wolker, A.; Villaescusa, L. A.; Diaz-Cabanas, M. J.; Valencia, S.; Cambor, M. A., Five-Coordinate Silicon in High-Silica Zeolites. *J. Am. Chem. Soc.* **1999**, 121, 3368-3376.
46. Fyfe, C. A.; Brouwer, D. H.; Lewis, A. R.; Chezeau, J. M., Location of the Fluoride Ion in Tetrapropylammonium Fluoride Silicalite-1 Determined by H-1/F-19/Si-29 Triple Resonance CP, REDOR, and TEDOR NMR Experiments. *J. Am. Chem. Soc.* **2001**, 123, 6882-6891.
47. Flanigen, E. M.; Bennett, J. M.; Grose, R. W.; Cohen, J. P.; Patton, R. L.; Kirchner, R. M.; Smith, J. V., Silicalite, a New Hydrophobic Crystalline Silica Molecular-Sieve. *Nature* **1978**, 271, 512-516.
48. Choi, M.; Na, K.; Kim, J.; Sakamoto, Y.; Terasaki, O.; Ryoo, R., Stable Single-Unit-Cell Nanosheets of Zeolite MFI as Active and Long-Lived catalysts. *Nature* **2009**, 461, 246-249.
49. Zhang, X.; Liu, D.; Xu, D.; Asahina, S.; Cychosz, K. A.; VaroonAgrawal, K.; AlWahedi, Y.; Bhan, A.; AlHashimi, S.; Terasaki, O.; Thommes, M.; Tsapatsis, M., Synthesis of Self-Pillared Zeolite Nanosheets by Repetitive Branching. *Science* **2012**, 336, 1684-1687.
50. Chaikittisilp, W.; Suzuki, Y.; Mukti, R. R.; Suzuki, T.; Sugita, K.; Itabashi, K.; Shimojima, A.; Okubo, T., Formation of Hierarchically Organized Zeolites by Sequential Intergrowth. *Angew. Chem. Int. Ed.* **2013**, 52, 3355-3359.
51. HoeKeoh, S.; Chaikittisilp, W.; Muraoka, K.; Mukti, R. R.; Shimojima, A.; Kumar, P.; Tsapatsis, M.; Okubo, T., Factors Governing the Formation of Hierarchically and Sequentially Intergrown MFI Zeolites by Using Simple Diquaternary Ammonium Structure-Directing Agents. *Chem. Mater.* **2016**, 28, 8997-9007.

52. Fleury, G.; Steele, J. A.; Gerber, I. C.; Jolibois, F.; Puech, P.; Muraoka, K.; HoeKeoh, S.; Chaikittisilp, W.; Okubo, T.; Roeffaers, M. B. J., Resolving the Framework Position of Organic Structure-Directing Agents in Hierarchical Zeolites via Polarized Stimulated Raman Scattering. *J. Phys. Chem. Lett.* **2018**, *9*, 1778-1782.
53. Villaescusa, L. A.; Li, J.; Gao, Z.; Sun, J.; Cambor, M. A., IDM-1: A Zeolite with Intersecting Medium and Extra-Large Pores Built as an Expansion of Zeolite MFI. *Angew. Chem. Int. Ed.* **2020**, *132*, 11379-11382.
54. Dib, E.; Gimenez, A.; Mineva, T.; Alonso, B., Preferential Orientations of Structure Directing Agents in Zeolites. *Dalton Trans.* **2015**, *44*, 16680-16683.
55. Cambor, M. A.; Villaescusa, L. A.; Díaz-Cabañas, M. J., Synthesis of All-Silica and High-Silica Molecular Sieves in Fluoride Media. *Top. Catal.* **1999**, *9*, 59-76.
56. Caulet, P.; Paillaud, J. L.; Simon-Masseron, A.; Soulard, M.; Patarin, J., The Fluoride Route: a Strategy to Crystalline Porous Materials. *C. R. Chimie* **2005**, *8*, 245-266.
57. Chao, K. J.; Lin, J. C.; Wang, Y.; Lee, G. H., Single-Crystal Structure Refinement of TPA ZSM-5 Zeolite. *Zeolites* **1986**, *6*, 35-38.
58. Ren, L.; Wu, Q.; Yang, C.; Zhu, L.; Li, C.; Zhang, P.; Zhang, H.; Meng, X.; Xiao, F. S., Solvent-Free Synthesis of Zeolites from Solid Raw Materials. *J. Am. Chem. Soc.* **2012**, *134*, 15173-14176.
59. Wu, Q.; Liu, X.; Zhu, L.; Ding, L.; Gao, P.; Wang, X.; Pan, S.; Bian, C.; Meng, X.; Xu, J.; Deng, F.; Maurer, S.; Müller, U.; Xiao, F. S., Solvent-Free Synthesis of Zeolites from Anhydrous Starting Raw Solids. *J. Am. Chem. Soc.* **2015**, *137*, 1052-1055.
60. Wu, Q.; Meng, X.; Gao, X.; Xiao, F. S., Solvent-Free Synthesis of Zeolites: Mechanism and Utility. *Acc. Chem. Res.* **2018**, *51*, 1396-1403.
61. Park, S. H.; Kunstleve, R. W. G.; Graetsch, H.; Gies, H., The Thermal Expansion of the Zeolites MFI, AFI, DOH, DDR, and MTN in their Calcined and As Synthesized Forms. *Stud Surf Sci Catal* **1997**, *105*, 1989-1994.
62. Dutta, P. K.; Puri, M., Synthesis and Structure of Zeolite ZSM-5 - A Raman Spectroscopic Study. *J. Phys. Chem.* **1987**, *91*, 4329-4333.
63. Bremard, C.; Laureyns, J.; Patarin, J., Polarized Single-Crystal Micro-Raman Spectroscopy of As-Synthesized Silicalite-1, Al MFI- and Fe MFI-Type Zeolites. *J. Raman Spectrosc.* **1996**, *27*, 439-445.
64. Fu, Y. Q.; Song, Y.; Huang, Y. I., An Investigation of the Behavior of Completely Siliceous Zeolite ZSM-5 under High External Pressures. *J. Phys. Chem. C* **2012**, *116*, 2080-2089.
65. Martinelli, A.; Creci, S.; Vavra, S.; Carlsson, P. A.; Skoglundh, M., Local Anisotropy in Single Crystals of Zeotypes with the MFI Framework Structure Evidenced by Polarised Raman Spectroscopy. *Phys. Chem. Chem. Phys.* **2020**, *22*, 1640-1654.
66. Mineva, T.; Dib, E.; Gaje, A.; Petitjean, H.; Bantignies, J.-L.; Alonso, B., Zeolite Structure Direction: Identification, Strength and Involvement of Weak CH $\cdots$ O Hydrogen Bonds. *ChemPhysChem* **2020**, *21*, 149-153.
67. Abraham, A.; Prins, R.; van Bokhoven, J. A.; van Eck, E. R. H.; Kentgens, A. P. M., TRAPDOR Double-Resonance and High-Resolution MAS NMR for Structural and Template Studies in Zeolite ZSM-5. *Solid State Nucl. Magn. Reson.* **2009**, *35*, 61-66.
68. Gougeon, R.; Delmotte, L.; Reinheimer, P.; Meurer, B.; Chezeau, J. M., High-Resolution Solid-State Nuclear Magnetic Resonance Study of the Tetrapropylammonium Template in a Purely Siliceous MFI-type Zeolite. *Magn. Reson. Chem.* **1998**, *36*, 415-421.

69. Dib, E.; Mineva, T.; Gaveau, P.; Alonso, B., N-14 Solid-State NMR: a Sensitive Probe of the Local Order in Zeolites. *Phys. Chem. Chem. Phys.* **2013**, *15*, 18349-18352.
70. Dib, E.; Mineva, T.; Alonso, B., Recent Advances in <sup>14</sup>N Solid-State NMR. *Ann. Rep. NMR Spectrosc.* **2016**, *66*, 175-235.
71. Martinez-Ortigosa, J.; Simancas, J.; Vidal-Moya, J. A.; Gaveau, P.; Rey, F.; Alonso, B.; Blasco, T., Host-Guest and Guest-Guest Interactions of P- and N-Containing Structure Directing Agents Entrapped inside MFI-Type Zeolite by Multinuclear NMR Spectroscopy. *J. Phys. Chem. C* **2019**, *123*, 22324-22334.
72. Larsen, F. H., Simulations of Molecular Dynamics in Solid-State NMR Spectra of Spin-1 Nuclei Including Effects of CSA- and EFG-Terms up to Second Order. *Solid State Nucl. Magn. Reson.* **2007**, *31*, 100-114.
73. Dib, E.; Mineva, T.; Gaveau, P.; Alonso, B., <sup>14</sup>N NMR of Tetrapropylammonium Based Crystals. *Eur. Phys. J. Special Topics* **2015**, *224*, 1769-1773.
74. Gougeon, R.; Chezeau, J. M.; Meurer, B., H-1 Solid-State Nuclear-Magnetic-Resonance Study of the Mobility of the Tetrapropylammonium Template in a Purely Siliceous Mfi-Type Zeolite. *Solid State Nucl. Magn. Reson.* **1995**, *4*, 281-293.
75. van Koningsveld, H.; van Bekkum, H.; Jansen, J. C., On the Location and Disorder of the Tetrapropylammonium (TPA) Ion in Zeolite ZSM-5 with Improved Framework Accuracy. *Acta Cryst. B* **1987**, *43*, 127-132.
76. Grosse-Kunstleve, R. W.; McCusker, L. B.; Baerlocher, C., Zeolite Structure Determination from Powder Diffraction Data: Applications of the FOCUS Method. *J. Appl. Cryst.* **1999**, *32*, 536-542.
77. Price, G. D.; Pluth, J. J.; Smith, J. V.; Bennett, J. M.; Patton, R. L., Crystal Structure of Tetrapropylammonium Fluoride Containing Precursor to Fluoride Silicalite. *J. Am. Chem. Soc.* **1982**, *104*, 5971-5977
78. Aubert, E.; Porcher, F.; Souhassou, M.; Petricek, V.; Lecomte, C., Location of Fluoride Counterion in As-Synthesized Silicalite-1 by Single Crystal X-ray Diffraction. *J. Phys. Chem. B* **2002**, *106*, 1110-1117.
79. Dib, E.; Alonso, B.; Mineva, T., DFT-D Study of N-14 Nuclear Quadrupolar Interactions in Tetra-alkyl Ammonium Halide Crystals. *J. Phys. Chem. A* **2014**, *118*, 3525-3533.
80. Sheldrick, G. M., Crystal Structure Refinement With SHELXL. *Acta Cryst. C* **2015**, *71*, 3-8.
81. Cadars, S.; Lesage, A.; Emsley, L., Chemical Shift Correlations in Disordered Solids. *J. Am. Chem. Soc.* **2005**, *127*, 4466-4476.
82. Engelhardt, G.; Michel, D., High-resolution solid-state NMR of silicates and zeolites. Wiley: Chichester, 1987.
83. Whitten, A. E.; Spackman, M. A., Anisotropic Displacement Parameters for H Atoms Using an ONIOM Approach. *Acta Cryst. B* **2006**, *62*, 875-888.
84. Sovago, I.; Gutmann, M. J.; Hill, J. G.; Senn, H. M.; Thomas, L. H.; Wilson, C. C.; Farrugia, L. J., Experimental Electron Density and Neutron Diffraction Studies on the Polymorphs of Sulfathiazole. *Cryst. Growth Des.* **2014**, *14*, 1227-1239.
85. Gies, H.; Marker, B., The Structure-Controlling Role of Organic Templates for the Synthesis of Porosils in the Systems SiO<sub>2</sub>/Template/H<sub>2</sub>O. *Zeolites* **1992**, *12*, 42-49.

86. Burkett, S. L.; Davis, M. E., Mechanisms of Structure Direction in the Synthesis of Pure-Silica Zeolites .1. Synthesis of Tpa/Si-Zsm-5. *Chem. Mater.* **1995**, *7*, 920-928.
87. Gómez-Hortigüela, L.; Camblor, M. A., Introduction to the Zeolite Structure-Directing Phenomenon by Organic Species: General Aspects. In *Insights into the Chemistry of Organic Structure-Directing Agents in the Synthesis of Zeolitic Materials. Structure and Bonding 175*, Gómez-Hortigüela, L.; Camblor, M. A., Eds. Springer: Cham, 2017; pp 1-41.
88. Al-Nahari, S.; Ata, K.; Mineva, T.; Alonso, B., Ubiquitous Presence of Intermolecular CH...O Hydrogen Bonds in As-synthesized Host-Guest Zeolite Materials. *Chem. Select* **2021**, *6*, 9728-9734.
89. Bell, R. G.; Jackson, R. A.; Catlow, C. R. A., Computer Simulation of the Monoclinic Distortion in Silicalite. *J. Chem. Soc., Chem. Commun.* **1990**, 782-783.
90. Grau-Crespo, R.; Acuaya, E.; Ruiz-Salvador, A. R., A Free Energy Minimisation Study of the Monoclinic–Orthorhombic Transition in MFI Zeolite. *Chem. Commun.* **2002**, 2544-2545.
91. Endoh, A., Calorimetric Study of the Monoclinic-Orthorhombic Phase Transition in Highly Siliceous Zeolite ZSM-5. *Zeolites* **1988**, *8*, 250-251.
92. van koningsveld, H.; Jansen, J. C.; van bekkum, H., The Orthorhombic Monoclinic Transition in Single-Crystals of Zeolite Zsm-5. *Zeolites* **1987**, *7*, 564-568.
93. van Koningsveld, H.; Jansen, J. C.; van Bekkum, H., The Monoclinic Framework Structure of Zeolite H-ZSM-5. Comparison with the Orthorhombic Framework of As-Synthesized ZSM-5. *Zeolites* **1990**, *10*, 235-242.
94. Marra, G. L.; Tozzola, G.; Leofanti, G.; Padovan, M.; Petrini, G.; Genoni, F.; Venturelli, B.; Zecchina, A.; Bordiga, S.; Ricchiardi, G., Orthorhombic and Monoclinic Silicalites: Structure, Morphology, Vibrational Properties and Crystal Defects. *Stud. Surf. Sci. Catal.* **1994**, *84*, 559-566.
95. Astala, R.; Auerbach, S. M.; Monson, P. A., Density Functional Theory Study of Silica Zeolite Structures: Stabilities and Mechanical Properties of SOD, LTA, CHA, MOR, and MFI. *J. Phys. Chem. B* **2004**, *108*, 9208-9215.
96. Zhang, J.; Lu, X.; Wang, Z., Control of Crystallization Rate and Morphology of Zeolite Silicalite-1 in Solvent-Free Synthesis. *Microporous Mesoporous Mater.* **2019**, *283*, 14-24.
97. Rodríguez-Carvajal, J., Recent Advances in Magnetic Structure Determination by Neutron Powder Diffraction. *Physica B* **1993**, *192*, 55-69.
98. Rodríguez-Carvajal, J., Recent Developments of the Program FULLPROF. *Commission on Powder Diffraction (IUCr). Newsletter* **2001**, *26*, 12-19.
99. Winn, M. D.; Ballard, C. C.; Cowtan, K. D.; Dodson, E. J.; Emsley, P.; Evans, P. R.; Keegan, R. M.; Krissinel, E. B.; Leslie, A. G. W.; McCoy, A.; McNicholas, S. J.; Murshudov, G. N.; Pannu, N. S.; Potterton, E. A.; Powell, H. R.; Read, R. J.; Vagin, A.; Wilson, K. S., Overview of The CCP4 Suite and Current Developments. *Acta Cryst. D* **2011**, *67*, 235-242.
100. Champsaur, A. M.; Yu, J.; Roy, X.; Paley, D. W.; Steigerwald, M. L.; Nuckolls, C.; Bejger, C. M., Two-Dimensional Nanosheets from Redox-Active Superatoms. *ACS Cent. Sci.* **2017**, *3*, 1050-1055.
101. Schreurs, A. M. M.; Lutz, M. *MERGEHKL5*, Laboratory for Crystal and Structural Chemistry, Bijvoet Center for Biomolecular Research, Utrecht, The Netherlands.

102. Momma, K.; Izumi, F., VESTA 3 for Three-Dimensional Visualization of Crystal, Volumetric and Morphology data. *J. Appl. Crystallogr.* **2011**, 44, 1272-1276.
103. Lesage, A.; Bardet, M.; Emsley, L., Through-Bond Carbon–Carbon Connectivities in Disordered Solids by NMR. *J. Am. Chem. Soc.* **1999**, 121, 10987-10993.
104. Bielecki, A.; Burum, D. P., Temperature Dependence of  $^{207}\text{Pb}$  MAS Spectra of Solid Lead Nitrate. An Accurate, Sensitive Thermometer for Variable-Temperature MAS. *J. Magn. Reson. A* **1995**, 116, 215-220.
105. Massiot, D.; Fayon, F.; Capron, M.; King, I.; Le Calve, S.; Alonso, B.; Durand, J. O.; Bujoli, B.; Gan, Z. H.; Hoatson, G., Modelling One- and Two-Dimensional Solid-State NMR Spectra. *Magn. Reson. Chem.* **2002**, 40, 70-76.
106. *DmFit* download page: <http://nmr.cemhti.cnrs-orleans.fr/Dmfit/>
107. Cadars, S.; Mifsud, N.; Lesage, A.; Epping, J. D.; Hedin, N.; Chmelka, B. F.; Emsley, L., Dynamics and Disorder in Surfactant-Templated Silicate Layers Studied by Solid-State NMR Dephasing Times and Correlated Line Shapes. *J. Phys. Chem. C* **2008**, 112, 9145-9154.
108. Cadars, S.; Lesage, A.; Pickard, C. J.; Sautet, P.; Emsley, L., Characterizing Slight Structural Disorder in Solids by Combined Solid-State NMR and First Principles Calculations. *J. Phys. Chem. A* **2009**, 113, 902-911.
109. Civalleri, B.; Zicovich-Wilson, C. M.; Valenzano, L.; Ugliengo, P., B3LYP Augmented with an Empirical Dispersion Term (B3LYP-D\*) as Applied to Molecular Crystals. *Cryst. Eng. Comm.* **2008**, 10, 405-410.
110. Grimme, S., Semiempirical GGA-Type Density Functional Constructed with a Long-Range Dispersion Correction. *J. Comput. Chem.* **2006**, 27, 1787-1799.
111. Yokomori, Y.; Idaka, S., The Structure of TPA-ZSM-5 with Si/Al=23. *Microporous Mesoporous Mater.* **1999**, 28, 405-413.
112. Gatti, C.; Saunders, V. R.; Roetti, C., Crystal-Field Effects on the Topological Properties of the Electron-Density in Molecular-Crystals - the Case of Urea. *J. Chem. Phys.* **1994**, 101, 10686-10696.
113. Nada, R.; Catlow, C. R. A.; Pisani, C.; Orlando, R., An Ab-Initio Hartree-Fock Perturbed-Cluster Study of Neutral Defects in LiF. *Modelling. Simul. Mater. Sci. Eng.* **1993**, 1, 165-187.
114. Peintinger, M. F.; Oliveira, D. V.; Bredow, T., Consistent Gaussian Basis Sets of Triple-Zeta Valence with Polarization Quality for Solid-State calculations. *J. Comput. Chem.* **2013**, 34, 451-459.
115. Simonov, A.; Goodwin, A., Designing Disorder into Crystalline Materials. *Nature Rev. Chem.* **2020**, 4, 657-673.